minerals

MDPI

Article

Multi-Stage Tungsten Mineralization: Insights from Scheelite Trace Elements and Geochronology of the Kalatawu–Kalasayi System (Western Tianshan, NW China)

Peng Yuan [1,2,*], Xuexiang Gu [1] and Yongmei Zhang [1]

[1] School of Earth Science and Resources, China University of Geosciences, Beijing 100083, China; xuexiang_gu@163.com (X.G.); zhangyongmei@cugb.edu.cn (Y.Z.)
[2] Zijin Mining Group Northwest Geological Exploration Co., Ltd., Urumqi 830035, China
* Correspondence: 3001180015@email.cugb.edu.cn; Tel.: +86-13565571632

Abstract

The Kalasayi tungsten deposit is a medium-sized quartz-vein scheelite tungsten deposit in the Western Tianshan, Central Asia Orogenic Belt. The Kalatawu pluton yielded Late Carboniferous zircon U–Pb ages (313.99–310.32 Ma), and molybdenite Re–Os dating gives an isochron age of 302.3 ± 1.8 Ma for W mineralization, indicating an ~8–12 Myr magmatic-hydrothermal system. Whole-rock geochemistry classifies the pluton as aluminous A_2-type granite formed in a post-collisional extensional setting. Zircon Hf isotopes ($\varepsilon Hf(t)$ = +2.8 to +8.3) suggest a mixed juvenile lower crust source with mantle input. In situ LA-ICP-MS scheelite trace element analysis and REE geochemistry distinguish two populations: proximal Group I (high Mo, low Sr, low ΣREE, right-inclined REE patterns) is precipitated from oxidizing magmatic fluid, and distal Group II (low Mo, high Sr, high ΣREE, flat REE patterns, strong positive Eu anomalies) records reduced, mixed fluid with intense fluid–rock interaction. Fluid inclusion data show decreasing temperature and salinity proximally to distally, confirming that mixing of magmatic and meteoric water led to cooling and pH increase that caused W precipitation. A four-stage metallogenic model is proposed for a post-collisional extensional setting, providing robust evidence for A-type granite-related, multi-stage W mineralization and establishing exploration indicators for the southwestern Central Asia Orogenic Belt.

Keywords: Kalatawu pluton; Kalasayi tungsten deposit; aluminous A_2-type granite; scheelite geochemistry; fluid inclusions; post-collisional extension; western Tianshan

1. Introduction

The Central Asian Orogenic Belt (CAOB) is the world's largest Phanerozoic accretionary orogen. It records a complete geodynamic evolution from subduction and closure of the Paleo-Asian Ocean, through microcontinent amalgamation and continent–continent collision to post-collisional extension since the Neoproterozoic. The CAOB hosts enormous mineral resources and thus constitutes the Central Asian Metallogenic Domain [1,2]. The Western Tianshan is located on the southwestern margin of the CAOB, between the Tarim Craton and the Tianshan-Yili Block. This belt experienced multiple stages of tectono-magmatic-metallogenic events and serves as a natural laboratory for studying the coupling between accretionary orogenesis and ore-forming systems.

Tungsten is a critical strategic metal and is closely related to granitic magmatism. In the Western Tianshan, a series of Late Paleozoic granite-related tungsten deposits,

Check for updates

Received: 5 July 2026
Revised: 23 July 2026
Accepted: 24 July 2026
Published: 27 July 2026

Copyright: © 2026 by the authors. Licensee MDPI, Basel, Switzerland. This article is an open access article distributed under the terms and conditions of the Creative Commons Attribution (CC BY) license.

including the Zuluhong and Kalasayi deposits, have been discovered, indicating significant metallogenic potential.

Recent research on tungsten deposits has made important progress. Such deposits are typically associated with highly fractionated granites emplaced in post-collisional extensional settings. Enrichment in incompatible elements (e.g., W, Sn, Mo, Nb, Ta) and volatiles (F, Cl, B) is key to forming large to giant tungsten deposits [3]. A-type granites formed in high-temperature, low-pressure post-collisional extensional environments can undergo high-degree fractional crystallization. This process leads to extreme enrichment of incompatible elements in the residual melt and subsequent exsolution of ore-forming fluids [4]. However, the identification of A-type granites is often challenged by overlapping geochemical signatures with highly fractionated I-type or S-type granites [5]. The Kalatawu pluton exhibits a complete intrusive sequence from mafic magmatic enclaves through granodiorite to porphyritic monzogranite, with tungsten mineralization spatially and temporally linked to the most evolved phases. This setting offers an ideal natural laboratory to test the A-type affinity and its causal relationship with tungsten mineralization (Figure 1).

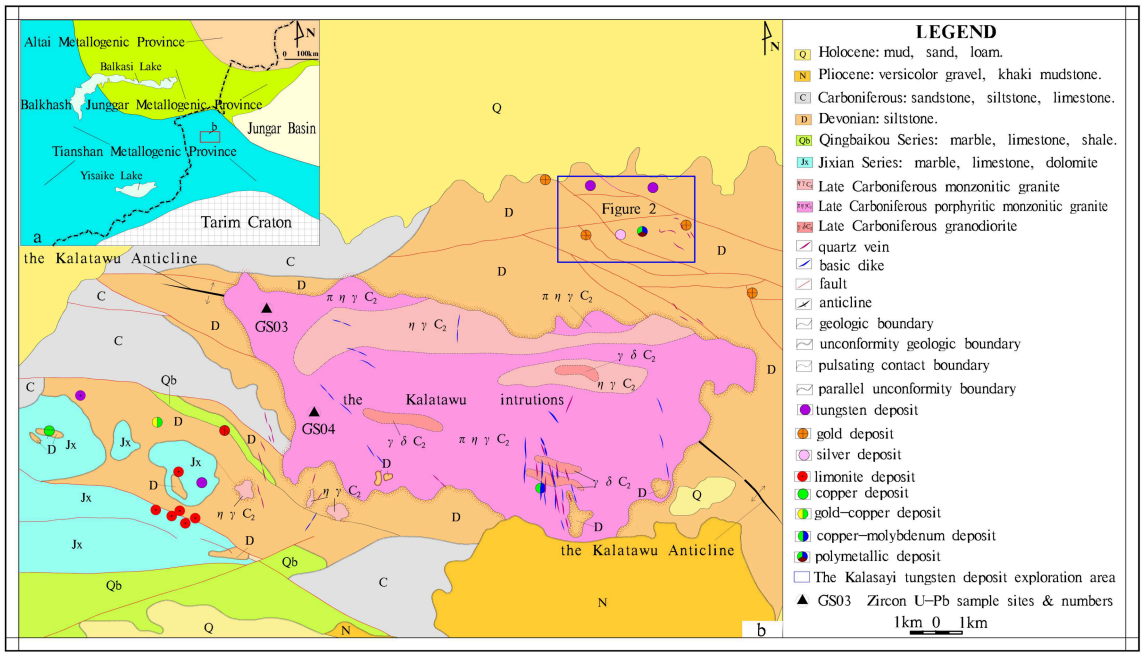


Figure 1. (**a**) Location of the study area in the Central Asian Orogenic Belt. (**b**) Regional geological map of the Kalasayi tungsten deposit, after Yuan et al. (2022) [6].

In situ scheelite ($CaWO_4$) geochemistry has recently become a powerful tool for tracing the source, evolution, and precipitation mechanisms of ore-forming fluids. The Ca^{2+} and W^{6+} sites in the scheelite lattice can be substituted by various trace elements, including REEs, Sr, Mo, and Nb, via isomorphism. The contents and ratios of these elements are controlled by fluid temperature, oxygen fugacity, salinity, and source characteristics and thus can "fingerprint" the mineralization process [7–10]. Despite previous studies on the geology and geochronology of the Kalasayi deposit [6,11], several critical issues remain unresolved. These include the precise petrogenetic type of the causative Kalatawu pluton (I-, S-, or A-type), the temporal relationship between magmatism and mineralization, the evolution path of ore-forming fluids and the controls on scheelite precipitation, and the geodynamic setting that favored both A-type magmatism and tungsten concentration.

Based on detailed field geological investigation, our study focuses on the Kalasayi tungsten deposit and the Kalatawu pluton. We employ zircon U-Pb geochronology, molybdenite Re-Os isotope dating, scheelite Sm-Nd isotope analysis, in situ LA-ICP-MS trace

element analysis, and fluid inclusion microthermometry. Our objectives are as follows. First, we aim to precisely determine the timing of magma emplacement and tungsten mineralization. Second, we investigate the petrogenesis, source characteristics, and tectonic setting of the causative pluton, with an emphasis on discriminating the granite type. Third, we characterize the physicochemical conditions, evolution, and sources of the ore-forming fluids. Fourth, we reveal the compositional zoning of scheelite and its implications for multi-stage mineralization. Fifth, we establish a genetic model linking A-type magmatism to tungsten deposition in a post-collisional extensional environment. The results provide a new case study for A-type granite-related W metallogeny in the CAOB and practical exploration criteria.

2. Regional and Deposit Geology

2.1. Regional Geological Framework

The Western Tianshan orogenic belt is bounded by the Junggar Block to the north and the Tarim Craton to the south. It comprises a complex collage of microcontinents, ophiolitic mélanges, volcanic arcs, and accretionary complexes. The study area is located in the Sayram microcontinent on the northern margin of the Western Tianshan [12], tectonically belonging to the Moynte-Alatau-Sayram metallogenic belt within the Tianshan metallogenic province. This area is an important polymetallic concentration zone in Western Tianshan, characterized by complex tectonic evolution and frequent magmatic activity.

Outcropping strata range from Proterozoic to Cenozoic. The Upper Devonian Tuosikuertaowu Formation (D_3ts) is the main host stratum for the Kalasayi tungsten deposit, consisting of littoral-neritic clastic rocks intercalated with pyroclastic rocks, mainly feldspar lithic sandstone, siltstone, and tuffaceous siltstone. This formation has a high background W content (up to 5 ppm), higher than crustal abundance, possibly providing some material source for mineralization. The Mesoproterozoic Jixian System Kusongmuqieke Group (J*xks*) is dominated by carbonate rocks and is a favorable host for Cu-Pb-Zn mineralization in the region.

The regional structural grain is generally NWW-SEE-trending. The main controlling structure is the Kusongmuqieken Fault, a long-lived regional tenso-shear fault that controlled magma emplacement and ore fluid migration, acting as the first-order fluid conduit. Secondary NW-trending faults and tensional fissures in the anticlinal core constitute the main ore-distributing and ore-hosting structures. The Kalatawu anticline is the regional main fold, with its core exposing the Upper Devonian Tuosikuertaowu Formation. The tensional fissures in the anticlinal axis provided favorable space for the emplacement of the Kalatawu pluton and the localization of tungsten ore bodies.

Regional magmatic activity was intense during the Middle-Late Hercynian, dominated by felsic intrusions. The Kalatawu pluton is the largest Carboniferous intrusion in the area, exposed as an irregular batholith covering about 80 km^2. Lithologies mainly include porphyritic monzogranite, medium-coarse grained monzogranite, coarse-grained K-feldspar granite, and granodiorite. This pluton intruded into the Upper Devonian Tuosikuertaowu Formation and formed a wide hornfels zone in the contact aureole. It is the causative pluton directly related to the Kalasayi tungsten mineralization [11]. Additionally, numerous NW-trending ore-bearing quartz veins developed in the area, serving as the main ore-hosting structures.

Regional mineralization is dominated by W, Au, Cu, Pb, and Zn, with associated Mo, Ag, etc. Tungsten deposits are mainly quartz-vein type and greisen type, concentrated in the contact zone of the Kalatawu pluton and peripheral fault zones. Representative deposits include the medium-sized Kalasayi and Zuluhong tungsten deposits [11,13–15]. Regional mineralization ages are concentrated in the Late Carboniferous to Early Permian

(310–285 Ma), highly coupled with tectono-magmatic events during the post-collisional extensional stage.

2.2. Deposit Geology

The Kalasayi tungsten deposit is located about 2 km northeast of the Kalatawu pluton. Orebodies are strictly controlled by NW-trending faults and interlayer fracture zones, occurring as veins and lenses. The main orebodies strike 310–320°, dip NE at 50–80°, and are 300–1500 m long and 0.5–8.5 m thick (average 2.3 m), with WO_3 grades ranging from 0.12% to 3.68% (average 1.05%). Orebody thickness and grade increase significantly near the pluton and decrease away from it, showing typical magmatic-hydrothermal control (Figure 2).

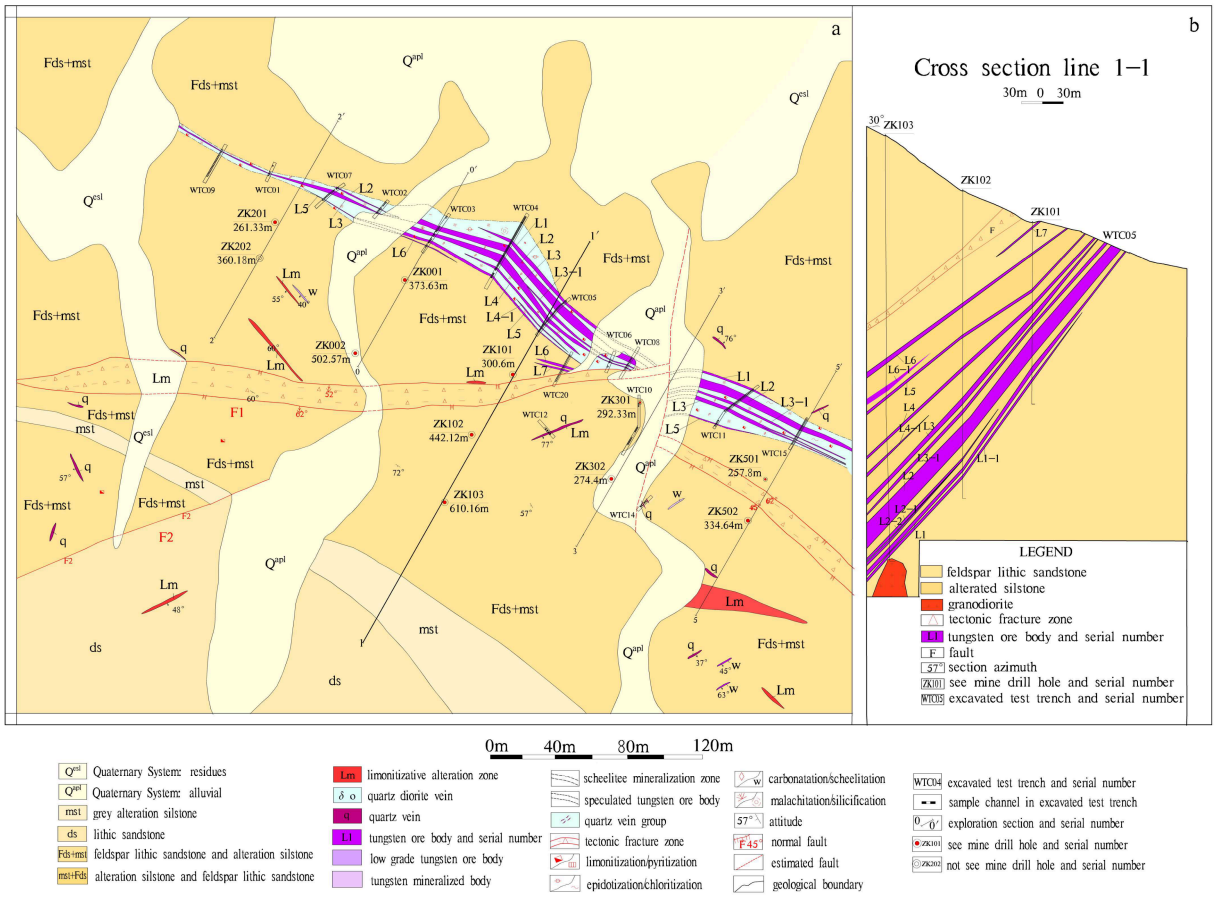


Figure 2. (**a**) Geological map of the Kalasayi tungsten deposit. (**b**) Cross section line 1-1 map of the Kalasayi tungsten deposit, after Yuan et al. (2022) [6].

The primary ore type is quartz-vein type scheeliteore (Group II (distal) scheelite, Figure 3A,F), with minor greisen-type and altered rock-type ore (Group I (proximal) scheelite, Figure 3D). Ore textures are mainly euhedral-subhedral granular and replacement textures. Structures are mainly massive, disseminated, and veinlet. Metallic minerals are mainly scheelite and molybdenite, followed by pyrite, chalcopyrite, galena, sphalerite, and bismuthinite. Gangue minerals are mainly quartz, followed by K-feldspar, plagioclase, sericite, chlorite, and calcite.

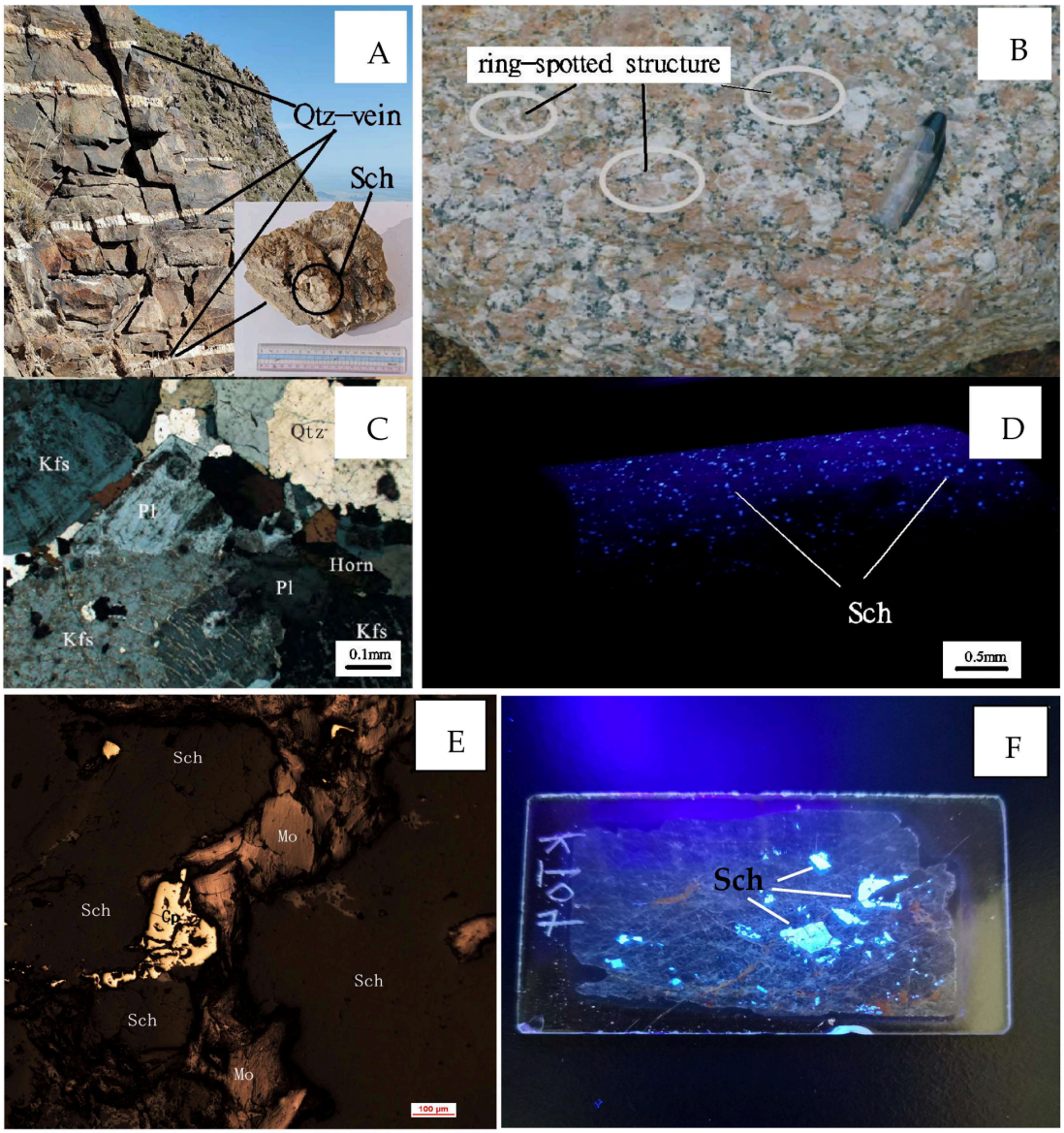


Figure 3. Representative photographs of hand specimens for (**A**) outcrops of scheelite quartz veins ; (**B**) coarse-grained ring-spotted structure biotite monzogranite in the Kalatawu pluton; (**C**) coarse-grained ring-spotted structure biotite monzogranite in thin section (Kfs + Qtz + Pl + Horn); (**D**) scheelite disseminated in granodiorite, in ZK001, 226.10 m, under ultraviolet lamp.); (**E**) photomicrographs of scheelite, chalcopyrite, and molybdenite under reflected light on polished sections; (**F**) Scheelite hosted in quartz veins, illuminated by a tungsten lamp. Abbreviations: Qtz, quartz; Kfs, K-feldspar; Pl, plagioclase; Horn, hornblende; Sch, scheelite; Mo, molybdenite; Cp, Chalcopyrite.

Based on macro-scale field cross-cutting criteria and micro-scale petrographic mineral assemblages, two generations of scheelite are distinguished. Group I (proximal) scheelite is fine-grained (<1 mm), anhedral to subhedral, occurring in quartz veins close to the pluton contact zone, and associated with molybdenite, pyrite, and minor chalcopyrite. Group II (distal) scheelite is coarse-grained (1–3 mm), euhedral to subhedral, found in quartz-carbonate veins farther from the pluton, and associated with fluorite, calcite, and minor sulfides.

Hydrothermal alteration is well-developed and shows clear spatial zoning. From the pluton contact zone outward, zones of potassic alteration, greisenization (muscovite + quartz), silicification, sericitization-chloritization, and carbonatization develop successively. Potassic alteration, greisenization, and silicification are proximal high-temperature alterations

most closely related to tungsten mineralization. High-grade ores are typically hosted in the strong alteration zones. Distal alterations are dominated by chloritization, carbonatization, and fluoritization.

Based on mineral assemblages, cross-cutting relationships, and fluid evolution characteristics, the mineralization process is divided into three periods [6]. The Magmatic Period (~314–310 Ma) involved emplacement and fractional crystallization of the Kalatawu pluton, providing the material and fluid basis for mineralization. The Hydrothermal Mineralization Period (~302–290 Ma) is further subdivided into a high-temperature potassic-greisen stage, a main ore-stage quartz-vein-scheelite stage, and a medium-low temperature alteration stage. The main ore stage represents the peak of tungsten precipitation. The supergene oxidation period formed limonite and caused minor damage to orebodies.

3. Samples and Analytical Methods

Our study systematically collected granite samples from the Kalatawu pluton, ore-bearing quartz-vein samples, scheelite separates, and wall rock samples, covering the pluton interior, contact zone, and proximal and distal mineralization zones.

3.1. Zircon U-Pb Dating and Hf Isotope Analysis

Two coarse-grained biotite monzogranite samples (GS03, GS04; sampling locations are shown in Figure 1) were selected for zircon separation. Zircon U–Pb dating and trace element and Hf isotope analyses were conducted by LA–ICP–MS at the State Key Laboratory of Geological Process and Mineral Resources (GPMR), China University of Geoscience, Beijing. The analyses parameter is 25 × 30 μm spot size, 10 nA intensity with 13 kV acceleration of focused O–primary beam. Zircon standard marked No. 91500 [16] was used to calibrate the raw data. Uncertainty of 1.5% (1RSD) for $^{206}Pb/^{238}U$ measurements was propagated for analysis [17]. All the results are reported at the 95% confidence level. The uncertainties of the ages reported are 1-sigma. The Isoplot program (Isoplot/Ex rev. 2.49) was used to calculate the LA–ICP–MS U–Pb ages. Zircon Hf isotopic analyses were carried out on the same grains previously analyzed for U–Pb dating using a Neptune multicollector ICP–MS connected to a Geolas 193 nm laser ablation system. The ablations parameters are 63 μm beam size, 26 s delayed, 10 Hz repetition rate, and 10 J/cm^2 energy density. The standard zircon GJ–1 yielded a mean $^{176}Hf/^{177}Hf$ ratio of 0.282009 ± 12 (n = 50) during the course of analysis, which was similar to the recommended value of 0.282000 ± 5 [18].

3.2. Molybdenite Re-Os Dating

Five molybdenite samples were collected from W-bearing quartz veins in drill holes Kzk102 and Kzk302. (The sample numbers and sampling locations are as follows: 18LE-ZK102-01, from 361.80 to 371.30 m; 18LE-ZK102-02, from 270.20 to 280.50 m; 18LE-ZK302-01, from 191.80 to 192.30 m; 18LE-ZK302-02, from 208.40 to 208.50 m; 18LE-ZK302-03, from 221.60 to 222.93 m; 18LE-ZK302-04, from 225.60 to 225.85 m.) Re–Os isotope analyses were performed at the Re–Os Laboratory, National Research Center for Geoanalysis, Chinese Academy of Geological Sciences, Beijing. The analytical procedures followed those outlined in [19]. The Carius tube method was used for the dissolution of molybdenite and equilibration of samples and tracers ^{185}Re and ^{190}Os at 230 °C for 10 h [20]. Os was recovered by distilling directly from the sample solution in the Carius tube and was subsequently purified by microdistillation. Re was recovered by ion exchange. The instrument used in this work was a TJA PQ Excell ICP mass spectrometer. The ^{187}Re-^{187}Os isochron age was calculated using Isoplot 4 version 4.1.

3.3. Whole-Rock Major and Trace Elements

Nineteen representative samples covering all four intrusive phases (mafic magmatic enclaves, granodiorite, coarse-grained biotite monzogranite, and porphyritic monzogranite) were analyzed for major and trace elements at the State Key Laboratory of Geological Processes and Mineral Resources (GPMR), China University of Geosciences (Beijing). Major elements were determined by X-ray fluorescence (XRF) on fused glass beads, with analytical precision better than 1%–2%. Trace elements, including REE, were analyzed by ICP-MS after acid digestion (HF + HNO_3), with precision and accuracy better than 5% for most elements [6].

3.4. Fluid Inclusion Microthermometry

Six quartz samples from the main ore stage (sample KLT03 from the upper part of ZK101, sample KLT04 from the middle part of ZK302, sample KLT06 from the bottom of ZK101, sample KLT07 from outcrop ore of trench WTC301, sample KLT10 from the middle part of ZK101, sample KLT15 from outcrop ore of section line 5) were used for fluid inclusion analysis. Doubly polished sections (0.2–0.3 mm thick) were prepared. Microthermometric measurements were performed at China University of Geosciences (Beijing) using a Linkam THMSG600 heating–freezing stage, calibrated with synthetic fluid inclusions. The measurement range was −196 to +600 °C, with precisions of ±0.1 °C (−100 to +25 °C), ±1 °C (25 to 400 °C), and ±2 °C (>400 °C). Salinities of aqueous inclusions were calculated using the equation of [21] for the H_2O-NaCl system. For CO_2-bearing inclusions, salinities were calculated from clathrate melting temperatures using the equation from [22]. Estimated trapping pressures for Type C inclusions were calculated using FLINCOR (Brown, 1989) [23], assuming a lithostatic pressure gradient of 27 MPa/km [24].

3.5. Scheelite In Situ Trace Elements and REEs

Five scheelite samples (sample KT01 from the bottom of ZK101, sample KT02 from outcrop ore of section line 5, sample KT03 outcrop ore of trench WTC301, sample KT05 from the upper part of ZK101, sample KT06 from the middle part of ZK102) were analyzed for trace elements and REEs by LA-ICP-MS at the National Geological Analysis Center in Beijing, China. A 193 nm ArF excimer laser coupled to an Agilent 7900 ICP-MS was used, with a spot size of 30 μm, a repetition rate of 8 Hz, and an energy density of 6 J/cm^2. NIST SRM 612 was used as the external standard, and Ca (as determined by electron microprobe) was used as the internal standard. Data reduction was performed using Iolite v4. Detection limits for most trace elements are <0.1 ppm.

3.6. Scheelite Sm-Nd Isotopes

Six scheelite samples (three from Group I, three from Group II) were analyzed for Sm-Nd isotopes using thermal ionization mass spectrometry (TIMS) at the Beijing Research Institute of Uranium Geology.

4. Results

4.1. Zircon U-Pb Geochronology

Zircon grains from samples GS03 and GS04 are euhedral and transparent and show clear oscillatory zoning, typical of magmatic origin [6]. Th/U ratios range from 0.48 to 3.02, also indicating a magmatic origin. U-Pb analyses yielded concordant to near-concordant ages. For sample GS03 (coarse-grained biotite monzogranite), 30 analyses yielded a weighted mean ^{206}Pb/^{238}U age of 310.32 ± 0.99 Ma (MSWD = 0.94) and a concordia age of 310.32 ± 0.99 Ma. For sample GS04, 30 analyses yielded a weighted mean age of 313.99 ± 0.72 Ma (MSWD = 1.0) and a concordia age of 313.99 ± 0.72 Ma. These ages are

interpreted as the emplacement ages of the Kalatawu pluton, indicating Late Carboniferous (Pennsylvanian) magmatism. Inherited zircon cores yield ages of 406–457 Ma (Silurian-Devonian), 734–986 Ma (Neoproterozoic), and 1341–1381 Ma (Mesoproterozoic), indicating the presence of Precambrian basement components in the magma source region [6].

4.2. Molybdenite Re-Os Geochronology

Six molybdenite samples from W-bearing quartz veins yielded Re concentrations ranging from 154 to 3767 ng/g and ^{187}Os concentrations from 1.4 to 36.9 ng/g. Common Os contents are very low (0.047–0.524 ng/g). The data define a well-correlated isochron with an age of 302.3 ± 1.8 Ma (MSWD = 0.49, initial $^{187}Os/^{188}Os$ = 0.3 ± 1.2). This is interpreted as the main stage of tungsten mineralization. The high Re content (up to 3767 ng/g) suggests a significant mantle contribution to the ore-forming materials. The ~8–12 Myr time gap between granite emplacement (314–310 Ma) and mineralization (302 Ma) reflects prolonged magmatic-hydrothermal evolution [6].

4.3. Whole-Rock Geochemistry of the Kalatawu Pluton

4.3.1. Major Elements

The rocks range from intermediate to felsic (SiO_2 = 48.7–77.3 wt %). The mafic magmatic enclaves (stage 1) have 48.7–67.1 wt % SiO_2, whereas the granodiorite (stage 2) has 61.3–62.5 wt % SiO_2. The coarse-grained biotite monzogranite (stage 3) and porphyritic monzogranite (stage 4) are more evolved, with SiO_2 = 69.4–77.3 wt %. Alkalis ($K_2O + Na_2O$) increase from 5.1–6.8 wt % (stage 1) to 7.0–8.9 wt % (stages 3–4). K_2O/Na_2O ratios rise from 0.38–0.61 (stage 1) to 1.07–1.54 (stage 4). CaO, MgO, TiO_2, and P_2O_5 decrease dramatically from stage 1 to stage 4 (CaO from 3.1–8.6 wt % to <2.0 wt %; MgO from 1.7–6.4 wt % to <0.5 wt %; TiO_2 from 0.7–2.2 wt % to <0.4 wt %; P_2O_5 from 0.16–0.27 wt % to <0.12 wt %). The iron index [FeO/(FeO + MgO) molar] is high (0.75–0.88) in evolved samples, indicating an iron-enriched, reduced nature. A/CNK ratios range from 0.94 to 1.29, mostly in the metaluminous to weakly peraluminous field, typical of aluminous A-type granites. On the SiO_2-K_2O diagram, samples plot in the high-K calc-alkaline series field [6].

4.3.2. Trace Elements and Rare Earth Elements

The evolved samples (stages 3–4) are enriched in high field strength elements (Zr = 98–243 ppm; Nb = 10.5–20.3 ppm; Y = 20.7–106 ppm; Ce = 42.9–127 ppm). The parameter Zr + Nb + Ce + Y ranges from 254 to 484 ppm, exceeding the 350 ppm threshold proposed by [18] for A-type granites. Ga contents (14–23 ppm) yield $10^4Ga/Al$ ratios of 2.6–3.5 (mostly >2.6). The rocks are strongly depleted in Sr (34–173 ppm), Ba (23–492 ppm), and Eu (δEu = 0.18–0.50), with Rb/Sr ratios up to 11.25. On primitive mantle-normalized spider diagrams, they show pronounced negative Ba, Sr, P, and Ti anomalies and no significant Nb-Ta negative anomaly. This feature is characteristic of A-type granites formed in extensional settings and precludes a subduction-related arc origin [6].

Total REE (ΣREE) increases from stage 1 (102–123 ppm) to stage 4 (120–312 ppm). Chondrite-normalized REE patterns of stages 3–4 are right-inclined with $(La/Yb)_n$ = 3.4–7.4 and display a pronounced negative Eu anomaly (δEu = 0.18–0.50), producing a "seagull-type" pattern typical of A-type granites. No significant tetrad effect is observed (TE1,3 and TE3,4 close to 1.0), indicating that extreme magmatic fractionation was not accompanied by fluid-melt interaction [6].

4.3.3. Zircon Hf Isotopes

In situ zircon Hf isotope analyses show $^{176}Hf/^{177}Hf$ ratios of 0.282670–0.282837, yielding positive εHf(t) values ranging from +2.8 to +8.3 (mostly > +5). Single-stage Hf model ages (TDM vary from 605 to 1714 Ma, and two-stage model ages (TDM2)) range from

782 to 1048 Ma for the Late Carboniferous zircons. These data indicate a juvenile lower crustal source derived from Neoproterozoic mafic protoliths, with minor contamination by ancient crust (as shown by a few inherited zircons with negative εHf(t) of −12 to −2 and TDM2 up to 2257 Ma). The Hf isotope compositions are consistent with an A_2-type granite derived from underplated basaltic lower crust in a post-collisional extensional setting [6].

4.4. Fluid Inclusion Characteristics

A total of 90 fluid inclusions in quartz from the main ore stage were examined (Table A1, Figures 4 and 5). Based on phase composition at room temperature, three types were identified.

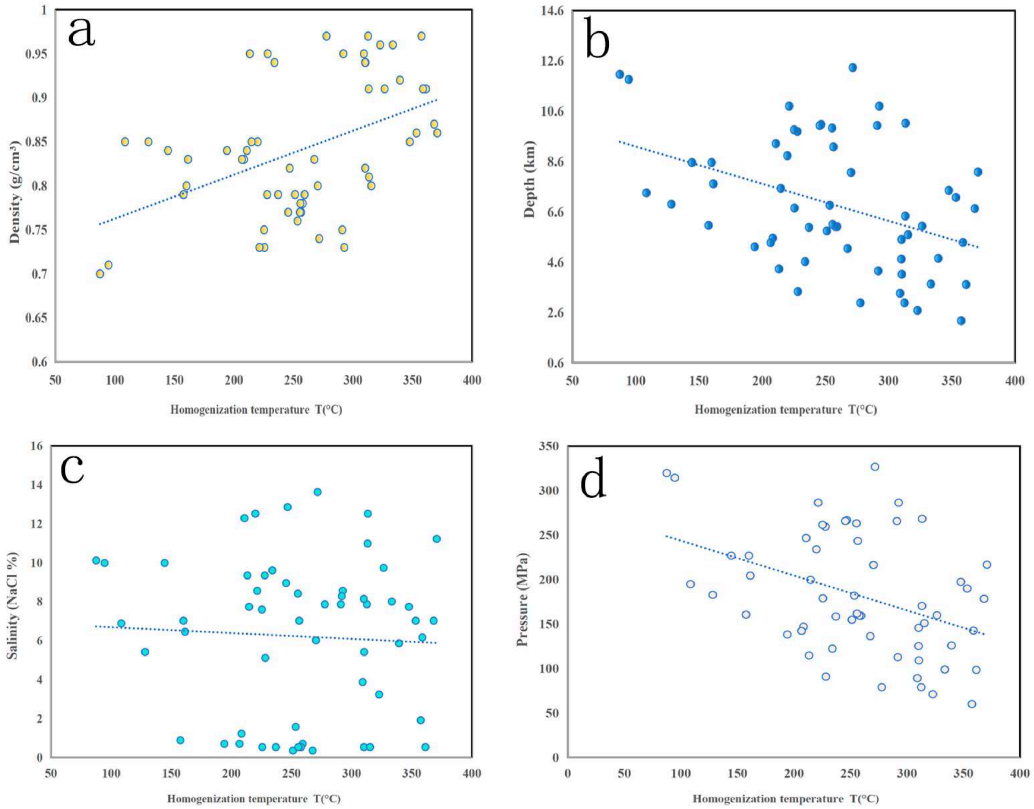


Figure 4. Schematic of the relationship between the homogenization temperature of fluid inclusions and density, depth, salinity, and pressure in the Kalasayi tungsten deposit. (**a**) Density vs. Homogenization temperature; (**b**) Depth vs. Homogenization temperature; (**c**) Salinity vs. Homogenization temperature; (**d**) Pressure vs. Homogenization temperature.

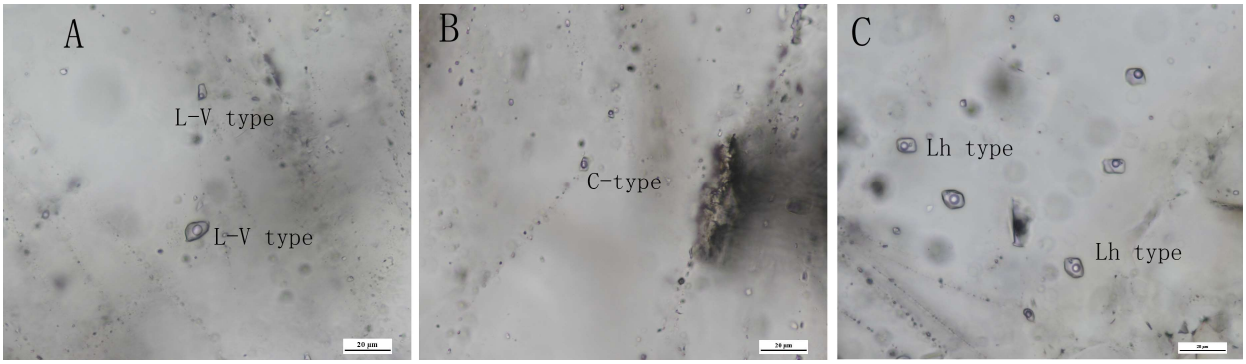


Figure 5. Microphotographs of fluid inclusions in the Kalasayi tungsten deposit ((**A**), liquid-vapor (L-V type); (**B**), CO_2-rich (C-type); (**C**), halite-bearing (L_h type)).

Type L-V (liquid-vapor two-phase) inclusions account for about 63% of the total. They are elliptical or irregular in shape and 2–20 μm in size, with vapor proportions of 15%–30%. Homogenization temperatures (Ths) range from 201.6 to 352.4 °C, with a main peak between 257 °C and 317 °C. Ice melting temperatures (Tm_ices) range from −10.0 to −0.2 °C, corresponding to salinities of 0.35–13.62 NaCl % equiv. (average 5.61 wt %). Densities range from 0.73 to 0.97 g/cm^3.

Type C (CO_2-bearing three-phase) inclusions account for about 36% of the total. They are negative crystal or elliptical in shape and 8–13 μm in size and are composed of liquid CO_2, vapor CO_2, and aqueous solution. First melting of CO_2 (Tm_CO_2) ranges from −64.1 to −51.4 °C, lower than the triple point of pure CO_2 (−56.32 °C), indicating the presence of volatiles such as CH_4 or N_2. CO_2 clathrate melting temperatures (Tm_claths) range from 5.6 to 9.1 °C, yielding salinities of 0.53–12.85 wt % NaCl equiv. Partial homogenization temperatures range from 23.6 to 30.3 °C. Total homogenization temperatures (Th_totals) range from 214.7 to 370.7 °C (average 317.2 °C), mostly homogenized to liquid.

Type Lh (daughter mineral-bearing multiphase) inclusions are rare, accounting for less than 1% of the total, and are only found in proximal samples. They consist of a halite daughter crystal, a vapor bubble, and liquid phase. The halite dissolution temperature is 379.2 °C, corresponding to extremely high salinity (>26.3 wt % NaCl equiv.), suggesting involvement of a highly saline magmatic fluid.

Trapping pressures for type C inclusions, estimated using FLINCOR (Brown, 1989) [23], range from 60 to 327 MPa. Assuming a lithostatic pressure gradient of 27 MPa/km, the corresponding depths range from 2.27 to 12.33 km (average 6.60 km). From the pluton contact zone outward (proximal to distal), homogenization temperatures decrease from about 317 °C to about 258 °C, and salinities decrease from 13.6 wt % to 5.6 wt %. This trend records progressive mixing of hot, saline magmatic fluid with cooler, dilute meteoric water.

4.5. Scheelite In Situ Trace Element and REE Geochemistry

LA-ICP-MS analyses were performed on 43 spots from five samples (KT01, KT02, KT03, KT05, KT06). Two distinct groups are clearly defined, consistent with petrographic observations (Tables A2 and A3, Figures 6 and 7).

Group I (proximal scheelite) includes samples KT01 and KT02. This group exhibits extremely high molybdenum concentrations ranging from 696 to 7459 parts per million, with an average value of approximately 3300 parts per million. Strontium contents are low, varying between 41 and 102 parts per million and averaging 68 parts per million. The total rare earth element concentrations are also low, spanning from 9 to 172 parts per million with a mean of 47 parts per million. The rare earth element patterns are right-inclined, as reflected by highly variable $(La/Yb)_n$ ratios between 4.1 and 100.9, indicating enrichment of light rare earth elements relative to heavy rare earth elements. Europium anomalies (δEu) range from 0.83 to 4.14 with an average of 1.32, displaying mostly weak negative to positive anomalies. Cerium anomalies (δCe) are highly variable between 0.42 and 22.18, averaging 5.9.

Group II (distal scheelite) includes samples KT03, KT05, and KT06. In contrast to Group I, this group shows very low molybdenum concentrations ranging from 33 to 60 parts per million, with an average of approximately 44 parts per million. Strontium contents are markedly elevated, varying between 142 and 400 parts per million and averaging 265 parts per million. The total rare earth element concentrations are significantly higher, spanning from 293 to 2328 parts per million with a mean value of approximately 800 parts per million. The rare earth element patterns are flat to slightly right-inclined, as indicated by $(La/Yb)_n$ ratios ranging from 0.34 to 18.5 and averaging 3.9. Europium anomalies (δEu) range from 0.90 to 5.14 with an average of 2.15, exhibiting consistently strong positive anomalies. Cerium anomalies (δCe) vary between 0.75 and 4.98, averaging 1.9, with most values near unity.

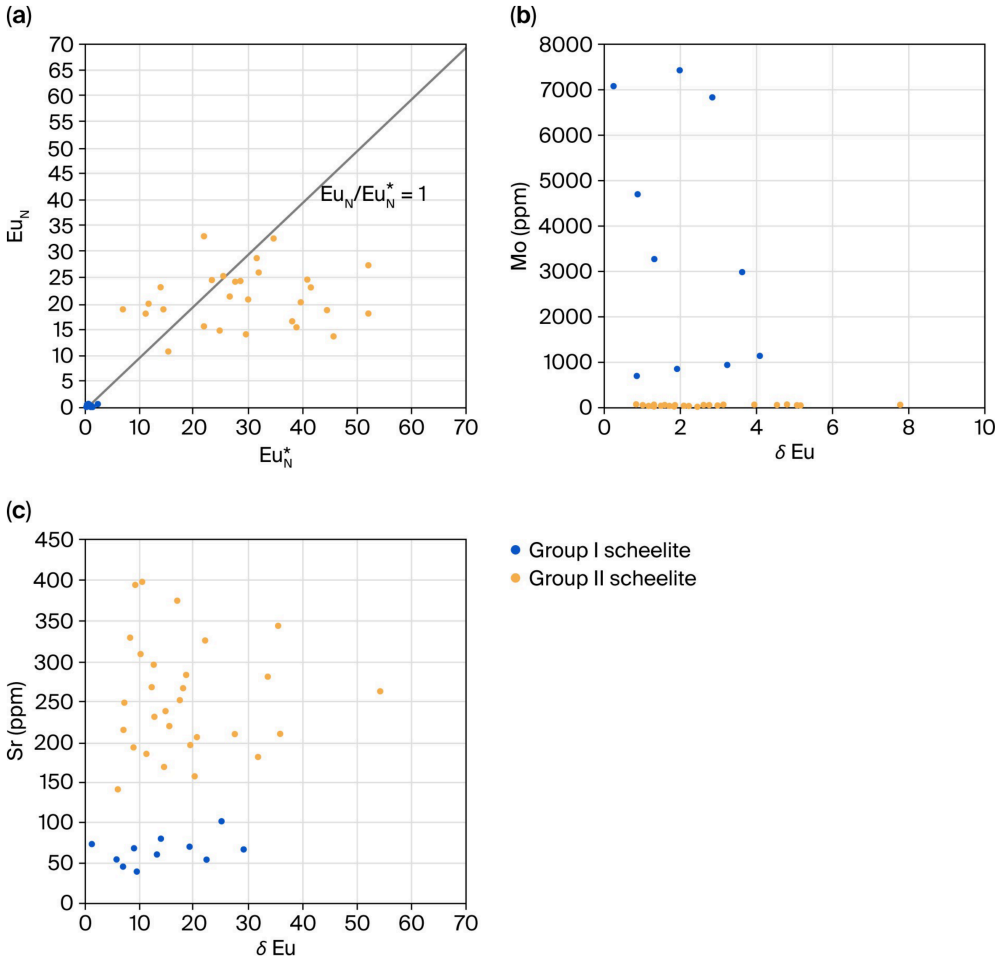


Figure 6. Graph of rare earth trace elements in scheelite of the Kalasayi tungsten deposit. (**a**) Eu_N vs. Eu_N^*; (**b**) Mo content vs. δEu; (**c**) Sr content vs. δEu.

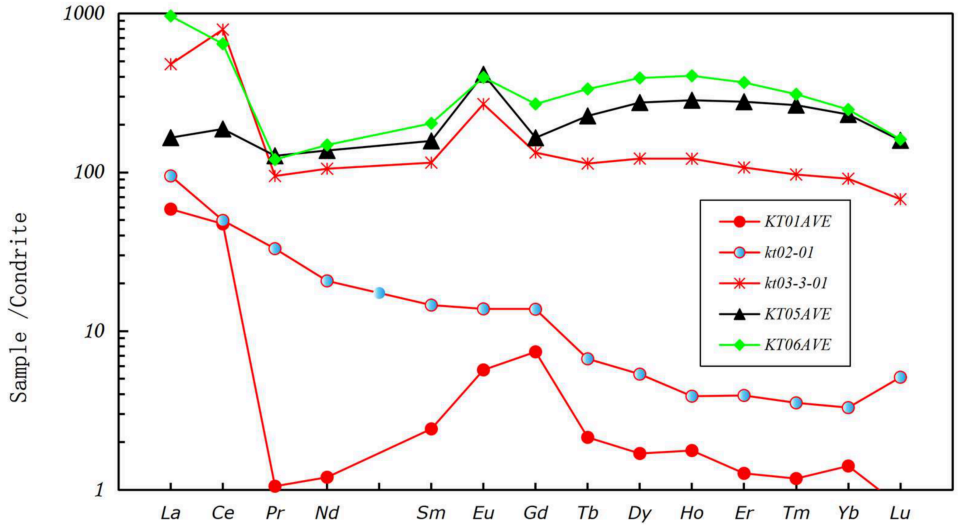


Figure 7. Chondrite-normalized rare earth element (REE) patterns for the scheelite samples from the Kalasayi tungsten deposit.

On the LREE-MREE-HREE ternary diagram (Figure 8), Group I scheelite plots near the LREE apex (greisen/porphyry field), whereas Group II shifts towards the MREE direction (vein field). On Mo-Sr and δEu-Sr discrimination diagrams, the two groups show clear boundaries (Figure 6).

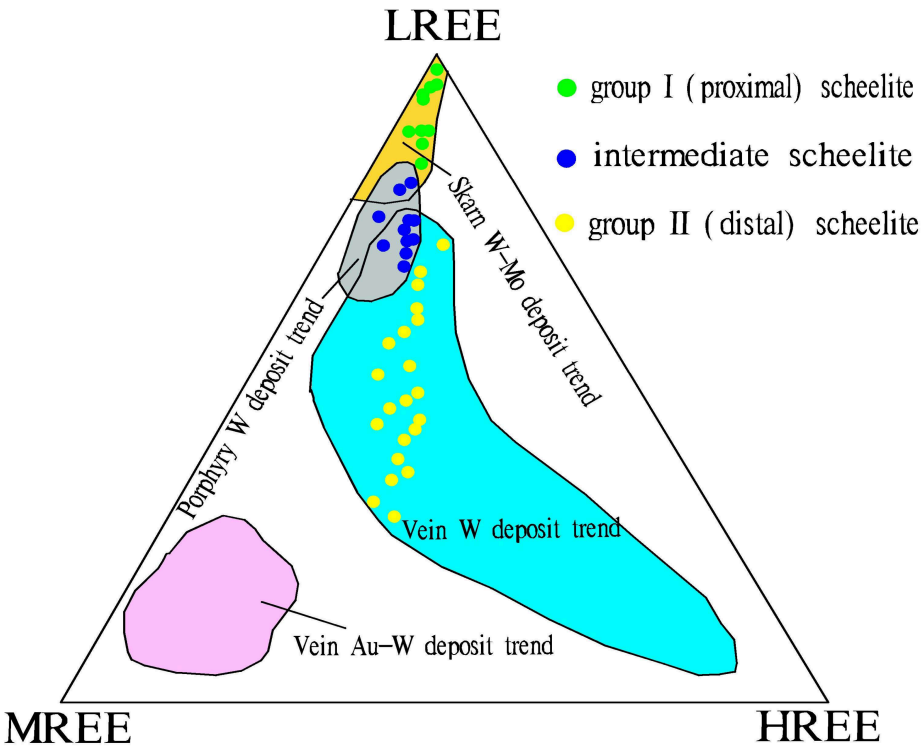


Figure 8. Schematic of mineralization type classification based on rare earth elements in scheelite of the Kalasayi tungsten deposit (green dots represent Group I (proximal) scheelite, yellow dots represent Group II (distal) scheelite, and blue dots represent intermediate scheelite.), after Wen et al. (2022) [25].

4.6. Sm-Nd Isotopes of Scheelite

Six scheelite samples (three from Group I, three from Group II) were analyzed. Sm contents range from 1.27 to 14.4 μg/g, Nd contents range from 4.52 to 38.9 μg/g, $^{147}Sm/^{144}Nd$ ratios range from 0.1693 to 0.2235, and $^{143}Nd/^{144}Nd$ ratios range from 0.512328 to 0.512609. The data points do not form a well-fitted isochron, with calculated "ages" ranging from 280 Ma to 340 Ma. This scatter indicates multi-stage mineralization and isotopic disequilibrium, consistent with the interpretation that scheelite formed from multiple hydrothermal pulses rather than a single closed system. Notably, the single-stage depleted mantle model age (TDM) of sample ZS04 is 302 Ma, consistent with the molybdenite Re-Os age, representing an important mineralization event [6].

5. Discussion

5.1. Discrimination of A-Type Granite and Exclusion of Highly Fractionated I-/S-Type

The Kalatawu pluton, especially its evolved phases (stages 3–4), exhibits a combination of geochemical features that are diagnostic of A-type granite rather than highly fractionated I-type or S-type [26]. These features include high $10^4Ga/Al$ ratios (>2.6, up to 3.5), which is a robust discriminant. Highly fractionated I-type granites may also have high Ga/Al, but they typically have lower HFSE contents (Zr + Nb + Ce + Y < 300 ppm) and show strong Nb-Ta negative anomalies, which are absent in our samples. The high Zr + Nb + Ce + Y values (254–484 ppm, average > 350 ppm) are well above the I-/S-type field. The lack of Nb-Ta depletion on primitive mantle-normalized spider diagrams precludes a subduction-related (arc) origin and supports an intraplate or post-collisional extensional setting.

The high FeO/(FeO + MgO) ratios (iron index > 0.8) indicate a ferroan composition, which is characteristic of A-type granites. The occurrence of primary ilmenite rather than magnetite, together with the presence of fluorite as an accessory mineral observed in thin sections, suggests crystallization under relatively reduced conditions and in a F-rich

environment—both features consistent with the petrogenesis of reduced A-type granites. The LREE enrichment with strong negative Eu anomalies produces a "seagull" REE pattern, distinct from the smoothly decreasing pattern of highly fractionated I-type. Zircon εHf(t) positive values (+2.8 to +8.3) indicate a juvenile crustal source, consistent with A_2-type formed by underplating in a post-collisional setting, whereas S-type would show negative εHf(t), and I-type could be positive but lacks the high HFSE. Thus, the Kalatawu pluton is unequivocally an aluminous A-type granite, belonging to the A_2 subtype, formed in a post-collisional extensional environment.

5.2. Timing of Magmatism and Mineralization: An ~8–12 Myr Magmatic-Hydrothermal System

The high-precision zircon U-Pb ages for the Kalatawu pluton (313.99 ± 0.72 Ma to 310.32 ± 0.99 Ma) and the molybdenite Re-Os isochron age (302.3 ± 1.8 Ma) obtained in [6] precisely define the temporal framework of the magmatic-hydrothermal system. The time gap of about 8–12 Myr between them is a typical feature of magmatic-hydrothermal tungsten deposits, reflecting the long-term evolution from magma emplacement, crystallization differentiation, and fluid exsolution to final ore precipitation. This time gap is similar to that observed in many world-class tungsten deposits, such as Panasqueira and Felbertal [27] and also comparable to the 5–15 Myr gaps documented in South China tungsten-tin systems (e.g., 150–160 Ma granites with 145–150 Ma mineralization) [28].

Regional tectonic evolution studies indicate that the Late Carboniferous (~320–310 Ma) was a critical period for the final collision between the Tarim Craton and the Tianshan-Yili Block [29], leading to significant crustal thickening. Subsequently, from the latest Carboniferous to the Early Permian (~310–280 Ma), the orogen entered a post-collisional extensional stage, characterized by lithospheric delamination and asthenospheric upwelling. This dynamic transition triggered partial melting of the lower crust, resulting in the formation of the Kalatawu pluton with typical aluminous A_2-type geochemical signatures. Therefore, the formation age of the Kalasayi tungsten deposit (~302 Ma) falls exactly within this post-collisional extensional time window. Together with the mineralization ages of other tungsten deposits in the region, such as the Zuluhong tungsten deposit (~284 Ma), they constitute a Late Carboniferous–Early Permian tungsten metallogenic event, demonstrating the existence of widespread post-collisional tungsten mineralization in the Western Tianshan during this period [30].

5.3. Magma Source and Metallogenic Potential

The highly fractionated aluminous A_2-type granite characteristics of the Kalatawu pluton, including high SiO_2, alkalis, Ga/Al, and strong negative Eu anomalies, together with positive zircon εHf(t) values (+2.8 to +8.3) and Neoproterozoic Hf model ages, collectively indicate that its magma source was dominated by juvenile lower crustal material. This juvenile crust likely originated from earlier underplating of mantle-derived magmas. The contamination by ancient crustal material (model ages up to 1714 Ma and inherited zircon cores with negative εHf(t) down to −12) suggests that the magma assimilated parts of the ancient basement of the Kazakhstan-Yili Plate during ascent or emplacement. This crust–mantle mixed source, particularly the addition of mantle components, provided the magmatic system with relatively high oxygen fugacity and abundant volatiles (e.g., F, Cl), which are crucial for the enrichment of tungsten as an incompatible element in the melt and for subsequent hydrothermal transport. Therefore, crust–mantle mixing and high-degree fractionation enrichment constitute the material basis for the formation of the Kalasayi tungsten deposit [6].

The prolonged magmatic-hydrothermal evolution (8–12 Myr) allowed extensive fractional crystallization to enrich W in the residual melt, development of a voluminous

hydrothermal circulation system, and progressive cooling and mixing with meteoric water, all of which were essential for the formation of a high resource potential tungsten deposit.

5.4. Source and Evolution of Ore-Forming Fluids

Integrating fluid inclusion data, we can outline the evolution path of the ore-forming fluids. The initial ore-forming fluids were high-temperature (>350 °C), moderately saline (10–13 wt % NaCl equiv.) magmatic water rich in W, Mo, F, Cl, etc., marked by the presence of Lh-type inclusions and the high Mo content of Group I scheelite. This fluid was oxidized, as indicated by the presence of Mo^{6+} substituting for W^{6+} in scheelite.

As these fluids migrated upward along structural fractures, pressure decrease caused CO_2 phase separation (immiscibility), as evidenced by abundant C-type inclusions. CO_2 loss increased fluid pH (due to removal of carbonic acid), which can promote scheelite precipitation because $CaWO_4$ solubility decreases with increasing pH under neutral-alkaline conditions. As the fluids moved farther from the pluton, they reacted with the overlying wall rocks, especially the Devonian clastic rocks and limestone of Jixian System Kusongmuqieke Group (J*xks*), and continuously mixed with downward-percolating, metal-poor meteoric water. This process led to a significant decrease in fluid temperature from about 317 °C proximally to about 258 °C distally, a decrease in salinity from 13–14 wt % to 5–6 wt % NaCl equiv., a decrease in oxygen fugacity, and an increase in pH. Thus, the ore-forming fluids evolved continuously from high-temperature magmatic fluids to medium-low-temperature mixed fluids.

5.5. Scheelite Precipitation and Multi-Stage Mineralization Mechanisms

The in situ geochemical characteristics of scheelite faithfully record the fluid evolution process and reveal different precipitation mechanisms.

Group I (proximal) scheelite has high Mo content and variable Eu anomalies (δEu mostly around 1.0), directly reflecting precipitation from an oxidizing magmatic fluid. Under oxidizing conditions, Mo exists as Mo^{6+}, which has a similar ionic radius and charge to W^{6+}, allowing easy substitution for W^{6+} in the scheelite lattice, resulting in high Mo enrichment. Meanwhile, Eu exists mainly as Eu^{3+}, which, due to its larger difference in radius and charge from Ca^{2+}, is less compatible in scheelite, leading to insignificant or weakly negative Eu anomalies. The precipitation of this scheelite group was primarily controlled by rapid cooling of the magmatic fluid near the pluton contact zone, possibly accompanied by pressure reduction and CO_2 degassing.

Group II (distal) scheelite has extremely low Mo content and a strong positive Eu anomaly (average δEu = 2.15, up to 5.14), indicating formation from a reduced mixed fluid that underwent intense wall–rock interaction. Under reducing conditions, Mo exists mainly as Mo^{4+}, which is incompatible with the W^{6+} site, resulting in very low Mo content. In contrast, Eu exists as Eu^{2+}, whose ionic radius is closer to that of Ca^{2+}, allowing it to readily enter the scheelite lattice and generate a strong positive Eu anomaly. The high Sr content also derives from fluid–rock interaction: the fluid reacted with Ca-rich wall rocks (e.g., plagioclase in Devonian siltstone and marble), leaching large amounts of Sr^{2+} into the fluid, which eventually precipitated in scheelite. The flat REE patterns of Group II scheelite, with $(La/Yb)_n$ around 3.9, are consistent with fluid–rock interaction that buffered LREE/HREE ratios to near-chondritic values.

The precipitation of Group II scheelite resulted from the coupling of multiple factors: continuous cooling ($\Delta T \approx 150$ °C), mixing with meteoric water (dilution), pH increase due to fluid–rock interaction and CO_2 loss, and decrease in oxygen fugacity. These factors collectively destabilized tungsten complexes in the hydrothermal fluid, such as WO_4^{2-} and WF_6^{2-}, leading to scheelite supersaturation and precipitation.

The scatter in Sm-Nd isotope ages (280–340 Ma), the multiple geochemical groups, and the cross-cutting relationships of multi-stage veins collectively demonstrate that the Kalasayi tungsten deposit experienced at least two significant hydrothermal mineralization events, making it a typical multi-stage superimposed deposit. The presence of rare Lh-type inclusions with extremely high salinity suggests that later hydrothermal pulses may have introduced additional fluids, contributing to the isotopic scatter.

5.6. Metallogenic Dynamic Model

Integrating geological, geochronological, geochemical, and fluid inclusion evidence, we propose a four-stage metallogenic dynamic model for the Kalasayi tungsten deposit.

Stage 1: Lithospheric delamination and crust–mantle mixing (~315–310 Ma). In the Late Carboniferous, continent–continent collision following the closure of the Paleo-Asian Ocean led to crustal thickening. Subsequently, the thickened lithosphere underwent delamination, triggering asthenospheric upwelling and underplating. The upwelling asthenosphere provided enormous heat and mantle-derived materials (volatiles) to the lower crust, causing partial melting of juvenile lower crustal material (Neoproterozoic mafic protoliths) and assimilation of some ancient crustal material. This process formed a crust–mantle mixed, W-rich, high-temperature magma.

Stage 2: A_2-type granite emplacement and fluid exsolution (~310 Ma). The crust–mantle mixed magma ascended along tenso-shear faults (e.g., the Kusongmuqieken Fault) and emplaced in favorable locations such as the anticlinal core, forming the Kalatawu A_2-type granite pluton at shallow to moderate depths (6–7 km). After emplacement, the magma underwent high-degree fractional crystallization, as recorded by the sequence from granodiorite to porphyritic monzogranite. This process involved separation of plagioclase, K-feldspar, apatite, and Fe-Ti oxides, leading to extreme enrichment of incompatible elements like W and Mo, as well as volatiles like H_2O and F, in the residual melt. When volatiles reached saturation, high-temperature (>350 °C), moderately saline (10–13 wt % NaCl equiv.), W-rich, oxidized magmatic fluids exsolved from the magma chamber.

Stage 3: Fluid ascent, mixing, and scheelite precipitation (between 302 and 310 Ma). The exsolved magmatic fluids migrated upward through the fracture system atop the pluton. During this ascent, pressure decrease caused CO_2 phase separation (immiscibility), raising fluid pH and causing initial scheelite precipitation (Group I) in the proximal contact zone (greisen-quartz-vein type). Further ascent allowed mixing with descending meteoric water, causing rapid cooling ($\Delta T \approx 150$ °C) and dilution, which drastically lowered scheelite solubility. In distal zones, the fluid interacted with marble wall rocks, gaining Ca and Sr, and becoming reduced due to Fe^{2+} buffering from mafic minerals. Under reduced conditions, Mo^{4+} was excluded from scheelite, Eu^{3+} was reduced to Eu^{2+} and strongly incorporated, and flat REE patterns were developed, producing Group II scheelite with low Mo, high Sr, and strong positive Eu anomalies. Late-stage molybdenite (~302 Ma) precipitated from the residual fluids (Figure 9).

Stage 4: Late-stage hydrothermal overprint. Subsequent hydrothermal pulses, some with higher salinity as indicated by rare Lh inclusions, remobilized and re-deposited scheelite. This late overprint caused the scatter in Sm-Nd isotope data and the complex cross-cutting vein relationships observed in the field.

5.7. Exploration Implications

The recognition that the Kalasayi deposit is related to a post-collisional aluminous A_2-type granite provides practical exploration criteria for tungsten deposits in the Tianshan orogen and similar settings elsewhere.

First, exploration should target Late Carboniferous to Early Permian (320–290 Ma) granites with A-type geochemical fingerprints. These include high SiO_2 (>69 wt %), high alkalis ($K_2O + Na_2O > 7$ wt %), high FeO/MgO (iron index >0.8), high Zr + Nb + Ce + Y (>350 ppm), high $10^4Ga/Al$ (>2.6), strong negative Eu anomalies (δEu < 0.3), and depletion in Sr, Ba, P, and Ti. The lack of Nb-Ta-negative anomalies is particularly important for discriminating A-type from arc-related I-type granites.

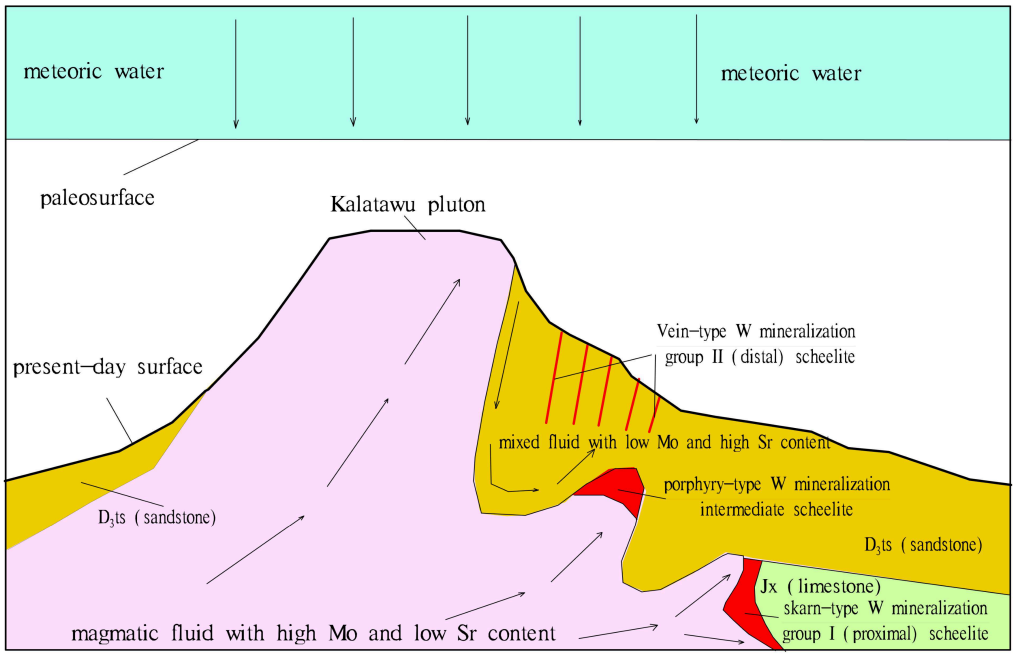


Figure 9. Cartoon diagram showing the integrated mineralization model.

Second, positive εHf(t) values in zircons (indicating juvenile crust with mantle input) are a favorable indicator for W-Sn mineralization, because such sources are enriched in incompatible elements. Third, the presence of a complete differentiation series from intermediate to highly felsic phases suggests efficient fractional crystallization, which is essential for W enrichment. The occurrence of mafic magmatic enclaves may indicate mantle input and magma mixing, which is also a positive sign.

Fourth, scheelite geochemistry can serve as a powerful vectoring tool. In distal exploration, low-Mo (<100 ppm), high-Sr (>200 ppm), strong positive Eu anomaly (δEu > 2) scheelite in float or stream sediments indicates a reduced, fluid–rock interaction-dominated environment, typical of distal halos. Proximal high-Mo (>1000 ppm), low-Sr (<100 ppm), weak Eu anomaly scheelite points closer to the source granite. The systematic decrease in Mo content and increase in Sr content and Eu anomaly from proximal to distal zones can help define the direction to the causative pluton.

Fifth, fluid inclusion surveys can provide additional vectors. Proximal zones contain abundant CO_2-bearing inclusions (C-type) and high-temperature L-V inclusions, whereas distal zones are dominated by low-salinity, low-temperature L-V inclusions. Mapping such fluid inclusion assemblages can help vector toward the source intrusion.

These exploration criteria are applicable to not only the Western Tianshan region but also other post-collisional orogenic belts worldwide where A-type granites are associated with tungsten mineralization.

6. Conclusions

First, the Kalatawu pluton, the causative intrusion of the Kalasayi tungsten deposit, is unequivocally an aluminous A-type granite (A_2 subtype), as evidenced by high SiO_2, high

alkalis, High FeO/MgO, high 10^4Ga/Al (>2.6), high Zr + Nb + Ce + Y (>350 ppm), strong negative Eu anomalies, seagull-type REE patterns, and lack of Nb-Ta depletion. Zircon Hf isotopes (εHf(t) = +2.8 to +8.3) indicate a juvenile lower crustal source with minor mantle input. The pluton formed in a post-collisional extensional setting related to lithospheric thinning and asthenospheric upwelling.

Second, high-precision geochronology defines the emplacement ages of the Kalatawu pluton at 313.99 ± 0.72 Ma to 310.32 ± 0.99 Ma (Late Carboniferous) and the main tungsten mineralization at 302.3 ± 1.8 Ma (Early Permian), yielding a ~8–12 Myr duration for the magmatic-hydrothermal system. This prolonged evolution allowed extensive fractional crystallization and fluid exsolution, which were key to the initial enrichment of tungsten.

Third, the ore-forming fluids evolved from an initial high-temperature (>350 °C), moderately saline (10–13 wt % NaCl equiv.), oxidized magmatic water to a cooler ($\Delta T \approx 150$ °C), lower-salinity (5–7 wt % NaCl equiv.), reduced mixed fluid through CO_2 phase separation and mixing with meteoric water. Fluid cooling, pH increase, and fluid–rock interaction were the main controls on large-scale scheelite precipitation. Oxygen fugacity controlled the partitioning of associated elements like Mo and Eu in scheelite.

Fourth, two compositionally distinct scheelite populations are identified. Group I (proximal) scheelite has high Mo (average ~3300 ppm), low Sr (average ~68 ppm), low ΣREE, right-inclined REE patterns, and weak Eu anomalies, precipitating from an oxidizing magmatic fluid. Group II (distal) scheelite has low Mo (average ~44 ppm), high Sr (average ~265 ppm), high ΣREE, flat REE patterns, and strong positive Eu anomalies (average δEu = 2.15), precipitating from a reduced mixed fluid after intense fluid–rock interaction. The geochemical differences between the two scheelite groups corroborate the fluid evolution path and multi-stage mineralization process.

Fifth, a four-stage metallogenic model is established for post-collisional A-type granite-related tungsten mineralization in the Western Tianshan region: (i) lithospheric delamination and crust–mantle mixed magmatism; (ii) A_2-type granite emplacement and exsolution of W-rich fluids; (iii) fluid ascent, cooling, mixing with meteoric water, and scheelite precipitation in structural traps; and (iv) late-stage hydrothermal overprint. This model provides a theoretical basis for understanding tungsten metallogenic regularity and guiding exploration in the Tianshan orogen and adjacent areas.

Finally, the combination of A-type geochemical fingerprints, positive εHf(t), and scheelite compositional zoning (especially Mo, Sr, and Eu anomalies) provides powerful vectoring tools for targeting hidden tungsten mineralization in post-collisional extensional settings.

Author Contributions: Conceptualization, P.Y. and X.G.; methodology, P.Y. and Y.Z.; software, P.Y.; validation, P.Y., X.G. and Y.Z.; formal analysis, P.Y.; investigation, P.Y.; resources, X.G.; data curation, P.Y.; writing—original draft preparation, P.Y.; writing—review and editing, X.G. and Y.Z.; visualization, P.Y.; supervision, X.G.; project administration, X.G.; funding acquisition, X.G. All authors have read and agreed to the published version of the manuscript.

Funding: This research was funded by Science and Technology Program of Xinjiang Uyghur Autonomous Region, China (grant no. 2023B03016), Deep Earth Probe and Mineral Resources Exploration-National Science and Technology Major Project (grant no. 2024ZD1001800), and the National Natural Science Foundation of China (grant no. 42130804 and 42573067).

Data Availability Statement: The data presented in this study are available on request from the corresponding author.

Conflicts of Interest: Peng Yuan is an employee of Zijin Mining Group Northwest Geological Exploration Co., Ltd. The paper reflects the views of the scientists and not the company.

Appendix A

Table A1. Summary table of fluid inclusion testing and comprehensive calculation results data for the Kalasayi tungsten deposit.

No.	Proj. No.	Measure Point No.	Host Mineral	Inclusion Type	Size (μm)		Gas Percentage (%)	Homogenization Temperature T (°C)	Freezing Point T (°C)	CO_2 Inclusion			Halite Dissolution Temperature T (°C)	Conclusion				Comment
					Long Axis	Minor Axis				First Melting Temperature T (°C)	CO_2 Clathrate Melting Temperature T (°C)	Patial Homogenization Temperature T (°C)		Salinity (%)	Pressure (MPa)	Density (g/cm^3)	Depth (km)	
1	KLT03	KLT03-01	Q	L-V	4	2	15	108.5	−3.1					6.88	194.75	0.85	7.35	
2		KLT03-02	Q	L-V	6	3	10	128.2	−3.3					5.41	182.79	0.85	6.90	
3		KLT03-03	Q	L-V	4	2	15	144.5	−3.6					9.98	226.84	0.84	8.56	
4		KLT03-04	Q	L-V	3	1	20	194.1	−4.4					0.70	138.18	0.84	5.21	
5		KLT03-05	Q	L-V	5	3	30	210.8	−4.9					12.28	246.61	0.84	9.31	
6		KLT03-06	Q	L-V	7	3	20	267.5	−5.8					0.35	136.33	0.83	5.14	
7		KLT03-07	Q	L-V	4	3	10	208.4	−4.9					1.22	147.03	0.83	5.55	
8		KLT03-08	Q	L-V	4	2	20	206.7	−4.4					0.70	142.18	0.83	5.37	
9		KLT03-09	Q	L-V	3	3	10	161.4	−3.8					6.45	204.30	0.83	7.71	
10	KLT04	KLT04-1	Q	Three-phase CO_2	3	2	35	312.6		−53.7	8.1	29.4		7.86	78.94	0.97	2.98	CO_2 inclusions are numerous, evidence for fluid immiscibility
11		KLT04-2	Q	Three-phase CO_2	5	3	30	309.1		−56.1	7.4	28.7		3.87	89.16	0.95	3.36	
12		KLT04-3	Q	Three-phase CO_2	3	3	30	310.2		−54.4	7.9	29		0.53	145.68	0.82	5.50	
13		KLT04-4	Q	Three-phase CO_2	4	3	40	313.4		−54.2	8.4	29.6		12.51	268.17	0.81	10.12	
14		KLT04-5	Q	Three-phase CO_2	3	2	40	315.3		−53.1	9.1	30.3		0.53	150.90	0.80	5.69	
15		KLT04-6	Q	L-V	3	2	10	270.3	−5.4					6.01	216.33	0.80	8.16	
16		KLT04-7	Q	L-V	4	3	20	277.7	−4.8					7.86	78.94	0.97	2.98	
17		KLT04-8	Q	Three-phase CO_2	3	3	30	357.4		−55.4	8.8	29.7		1.91	60.10	0.97	2.27	
18		KLT04-9	Q	Three-phase CO_2	5	3	40	322.8		−53.3	9.1	29.8		3.23	71.13	0.96	2.68	
19		KLT04-10	Q	Three-phase CO_2	3	2	40	333.4		−53.8	8.9	29.9		8.00	98.83	0.96	3.73	
20		KLT04-11	Q	L-V	4	3	20	292.6	−5.5					8.55	286.31	0.73	10.80	
21		KLT04-12	Q	L-V	3	2	20	246.7	−3.7					12.85	266.73	0.82	10.07	
22		KLT04-13	Q	L-V	6	1	20	228.2	−4					5.11	90.94	0.95	3.43	
23		KLT04-14	Q	L-V	3	3	20	213.3	−4.3					9.34	114.63	0.95	4.33	

https://doi.org/10.3390/min16080782

Table A1. *Cont.*

No.	Proj. No.	Measure Point No.	Host Mineral	Inclusion Type	Size (μm)		Gas Percentage (%)	Homogenization Temperature T (°C)	Freezing Point T (°C)	CO_2 Inclusion			Halite Dissolution Temperature T (°C)	Conclusion				Comment
					Long Axis	Minor Axis				First Melting Temperature T (°C)	CO_2 Clathrate Melting Temperature T (°C)	Patial Homogenization Temperature T (°C)		Salinity (%)	Pressure (MPa)	Density (g/cm^3)	Depth (km)	
24		KLT06-01	Q	L-V	5	3	10	160.1	−0.3					7.02	226.77	0.80	8.56	
25		KLT06-02	Q	L-V	6	4								8.81	247.65	0.80	9.35	
26		KLT06-03	Q	L-V	8	2								0.35	152.00	0.80	5.74	
27		KLT06-04	Q	L-V	4	3	30	157.6						0.88	160.51	0.79	6.06	
28		KLT06-05	Q	L-V	5	3	30	259.3	−0.3					0.70	159.34	0.79	6.01	
29		KLT06-06	Q	L-V	6	4	10	251.2	−0.2					0.35	154.73	0.79	5.84	
30		KLT06-07	Q	L-V	5	4	20							0.70	160.03	0.79	6.04	
31		KLT06-08	Q	L-V	8	4	10	227.8	−0.4					9.34	259.41	0.79	9.79	
32		KLT06-09	Q	L-V	4	4	15	237	−0.3					0.53	158.46	0.79	5.98	
33		KLT06-10	Q	L-V	3	2	20	257.8	−0.3					0.53	159.39	0.78	6.01	
34		KLT06-11	Q	L-V	5	1.5	10	255.7	−0.2					0.53	161.66	0.78	6.10	
35		KLT06-12	Q	L-V	4	2	10	256.4	−0.4					7.02	243.31	0.77	9.18	
36	KLT06	KLT06-13	Q	L-V	4	3	10	245.5	−0.3					8.95	265.79	0.77	10.03	
37		KLT06-14	Q	L-V	4	3	10	255.3	−0.4					8.41	263.10	0.77	9.93	
38		KLT06-15	Q	L-V	4	3	10	253.4	−0.5					1.57	181.84	0.76	6.86	
39		KLT06-16	Q	Three-phase CO_2	4	4	40	291.8		−60.3	7.7	29.4		8.28	112.70	0.95	4.25	Homogenized to liquid CO_2
40		KLT06-17	Q	Three-phase CO_2	5	4	30	234		−61.8	7.3	29.7		9.60	122.33	0.94	4.62	
41		KLT06-18	Q	Three-phase CO_2	4	2	45	310.4		−61.4	7.5	28.7		5.41	109.15	0.94	4.12	
42		KLT06-19	Q	L-V	3	1.5	20	225.3	−0.2					7.59	261.42	0.75	9.86	
43		KLT06-20	Q	L-V	5	3	15	291	−0.3					7.86	265.69	0.75	10.03	
44		KLT06-21	Q	L-V	4	2	10	271.6	−0.9					13.62	326.69	0.74	12.33	
45		KLT06-22	Q	L-V	4	3	15	225.6	−0.7					0.53	178.87	0.73	6.75	
46		KLT06-23	Q	L-V	3	2	15	263	−0.3									
47		KLT06-24	Q	L-V	3	3	15	221.4	−0.4					8.55	286.31	0.73	10.80	
48		KLT07-01	Q	L-V	10	8	5	94.6	−1.9					9.98	314.32	0.71	11.86	
49		KLT07-02	Q	L-V	2	2	20	87.5	−1.1					10.11	319.64	0.70	12.06	
50		KLT07-03	Q	L-V	2	2	10	114	−2.3									
51		KLT07-04	Q	Three-phase CO_2	7	3	30	310.1		−54.6	8.9	29.8		8.14	125.18	0.94	4.72	
52	KLT07	KLT07-05	Q	Three-phase CO_2	4	4	50	339.3		−56.3	8.3	28.5		5.86	125.81	0.92	4.75	
53		KLT07-06	Q	Three-phase CO_2	4	2	30	326.5		−55.3	8.7	29.2		9.73	159.80	0.91	6.03	
54		KLT07-07	Q	L-V	4	2	20	130	−5.2									
55		KLT07-08	Q	L-V	4	2	15	246.8	−4.4									
56		KLT07-09	Q	L-V	3	3	30	264.8	−4.4									
57		KLT07-10	Q	L-V	3	3	30	257.3	−6.1									

Table A1. *Cont.*

No.	Proj. No.	Measure Point No.	Host Mineral	Inclusion Type	Size (μm)		Gas Percentage (%)	Homogenization Temperature T (°C)	Freezing Point T (°C)	CO_2 Inclusion			Halite Dissolution Temperature T (°C)	Conclusion				Comment
					Long Axis	Minor Axis				First Melting Temperature T (°C)	CO_2 Clathrate Melting Temperature T (°C)	Patial Homogenization Temperature T (°C)		Salinity (%)	Pressure (MPa)	Density (g/cm^3)	Depth (km)	
58		KLT10-01	Q	Three-phase CO_2	2	2	40	319		−64.1	7.7	29.3						
59		KLT10-02	Q	Three-phase CO_2	2	2	50	313.2		−63.7	7.9	29.6		10.98	170.33	0.91	6.43	
60		KLT10-03	Q	Three-phase CO_2	4	3	40	361.3		−53.2	8.3	30		0.53	98.41	0.91	3.71	
61		KLT10-04	Q	Three-phase CO_2	6	4	35	358.7		−52.8	8.1	29.9		6.16	142.53	0.91	5.38	
62		KLT10-05	Q	L-V	2	2	20	250.5	−5.7									
63		KLT10-06	Q	L-V	2	1.5	20	304.7	−6.6									
64		KLT10-07	Q	L-V	2	1	10	308.5	−6.7									
65		KLT10-08	Q	L-V	2	1.5	10	312.1	−6.9									
66	KLT10	KLT10-09	Q	Three-phase CO_2	4	3	30	368.1		−52.3	8.3	29.9		7.02	178.35	0.87	6.73	
67		KLT10-10	Q	Three-phase CO_2	3	3	40	370.7		−51.4	8.5	30.1		11.22	216.69	0.86	8.18	
68		KLT10-11	Q	Sub-mineral phases	6	4	10	379.2					312.3	The subcrystals containing NaCl (the initial melting temperature and the temperature at which melting is completed and a molten state is achieved)				
69		KLT10-12	Q	Three-phase CO_2	4	4	30	353.2		−53.3	8.2	29.8		7.02	189.93	0.86	7.17	
70		KLT10-13	Q	Three-phase CO_2	5	4	30	347.6		−54	8.7	30.2		7.73	197.32	0.85	7.45	
71		KLT10-14	Q	L-V	5	3	20	315.4	−5.2									
72		KLT10-15	Q	L-V	3	3	30	352.4	−5.4									
73		KLT10-16	Q	L-V	4	2	20	279	−5									
74		KLT10-17	Q	L-V	2	1	20	326.7	−5.3									
75		KLT15-01	Q	L-V	2	1	10	82.9	−5	It is obvious that the two generations have significant differences in morphology and homogenization temperature. Those with a temperature lower than 200 °C are mostly needle-like in structure and larger in size; those with a temperature higher than 250 °C are mostly elliptical or irregular rectangular and also larger; while those with a temperature lower than 150 °C are mostly long elliptical in shape and smaller, possibly being secondary inclusions							
76		KLT15-02	Q	L-V	4	2	20	283.3	−9.7									
77		KLT15-03	Q	L-V	3	3	10	159.7	−7.4									
78		KLT15-04	Q	L-V	4	3	10	222.1	−8.5									
79		KLT15-05	Q	L-V	2	1	20	120.2	−6.3									
80		KLT15-06	Q	L-V	4	3	10	113.7	−6.1									
81		KLT15-07	Q	L-V	7	3	20	239.9	−8.7									
82	KLT15	KLT15-08	Q	L-V	6	4	10	236.3	−9									
83		KLT15-09	Q	L-V	6	3	20	316.8	−10									
84		KLT15-10	Q	Three-phase CO_2	8	2	20	219.9		−62.8	5.6	26.4		12.51	233.96	0.85	8.83	
85		KLT15-11	Q	Three-phase CO_2	5	3	20	214.7		−60.3	6	23.6		7.73	199.60	0.85	7.53	
86		KLT15-12	Q	L-V	3	2	30	209.3	−8.7									
87		KLT15-13	Q	L-V	6	3	20	201.6	−7.6									
88		KLT15-14	Q	L-V	6	3	20	156.3	−6.4									
89		KLT15-15	Q	L-V	4	2	20	116.4	−5.3									
90		KLT15-16	Q	L-V	3	1	20	103.2	−5.1									

Table A2. REEs in scheelite from the Kalasayi tungsten deposit, Western Tianshan, Xinjiang.

Sample	Point	La	Ce	Pr	Nd	Sm	Eu	Gd	Tb	Dy	Ho	Er	Tm	Yb	Lu	Y	ΣREE	LREE	HREE	LREE /HREE	LaN /YbN	δ Eu	δ Ce	t1	t3	t4	TE1,3	TE3,4
KT01	kt01-01	24.16	143.13	0.10	0.53	0.41	0.75	0.99	0.06	0.72	0.18	0.26	0.03	0.17	0.01	2.64	171.50	169.09	2.41	70.15	100.88	3.58	22.18	1.48	0.55	1.45	0.90	0.89
	kt01-02	5.64	1.88	0.22	0.91	0.43	0.16	0.80	0.05	0.28	0.08	0.18	0.01	0.26	0.02	1.58	10.93	9.24	1.68	5.49	15.35	0.83	0.42	0.39	0.53	0.82	0.45	0.66
	kt01-03	47.76	85.67	0.21	1.03	0.34	0.12	8.32	0.03	0.03	0.07	0.11	0.00	0.00	0.00	0.68	143.69	135.14	8.56	15.79	3.39	0.22	6.63	0.83	0.04	0.82	0.19	0.19
	kt01-04	5.61	1.58	0.07	0.74	0.23	0.19	0.18	0.01	0.19	0.06	0.03	0.01	0.18	0.01	0.81	9.10	8.41	0.68	12.34	21.98	2.77	0.63	0.22	0.51	3.76	0.33	1.38
	kt01-05	6.71	13.01	0.07	0.56	0.10	0.14	0.48	0.04	0.21	0.04	0.15	0.00	0.00	0.00	0.65	21.51	20.58	0.92	22.27	4.08	1.99	4.81	0.66	0.72	3.76	0.69	1.65
	kt01-06	3.97	1.02	0.02	0.23	0.20	0.43	0.52	0.09	0.68	0.18	0.49	0.11	0.54	0.13	4.46	8.62	5.87	2.75	2.13	5.27	4.14	0.98	0.19	0.90	0.97	0.41	0.93
	kt01-07	5.04	6.93	0.16	0.41	0.33	0.29	0.24	0.07	0.31	0.09	0.15	0.03	0.14	0.00	1.81	14.20	13.17	1.04	12.70	25.36	3.20	1.88	1.02	1.07	4.10	1.04	2.09
	kt01-08	10.72	3.65	0.08	0.50	0.87	0.52	1.54	0.25	0.97	0.12	0.28	0.02	0.24	0.01	2.63	19.78	16.35	3.43	4.76	32.25	1.38	0.97	0.32	1.24	1.72	0.63	1.46
	KT01-09	15.47	3.90	0.01	0.12	0.45	0.32	0.59	0.08	0.49	0.07	0.25	0.01	0.60	0.02	2.33	22.39	20.27	2.13	9.54	18.58	1.92	3.09	0.16	1.07	1.23	0.41	1.14
	AVERAGE	13.90	28.97	0.10	0.56	0.37	0.33	1.52	0.08	0.43	0.10	0.21	0.03	0.24	0.02	1.95	46.86	44.24	2.62	16.87	41.96	1.32	5.94	0.85	0.51	1.16	0.66	0.77
KT02	kt02-01	22.50	30.46	3.14	9.67	2.23	0.80	2.82	0.25	1.36	0.22	0.65	0.09	0.56	0.13	7.69	74.89	68.79	6.09	11.29	28.63	0.97	0.89	0.91	0.82	0.78	0.87	0.80
KT03	kt03-01	101.88	2094.28	6.54	25.15	8.44	17.94	15.20	2.25	16.97	4.70	14.19	1.87	17.27	1.82	190.23	2328.47	2254.23	74.25	30.36	4.23	4.84	19.90	3.19	0.81	1.10	1.61	0.94
	kt03-02	84.85	118.79	7.23	39.09	13.05	10.62	18.38	3.41	24.14	5.22	13.09	1.70	12.37	1.30	158.77	353.25	273.62	79.62	3.44	4.92	2.10	1.18	0.70	1.03	1.10	0.85	1.06
	kt03-03	100.30	109.30	7.67	43.13	13.92	18.82	15.35	3.05	19.35	4.36	12.04	1.74	12.83	1.28	162.20	363.14	293.14	70.00	4.19	5.61	3.94	0.97	0.61	1.04	1.18	0.79	1.11
	kt03-07	193.53	239.56	13.43	81.12	33.43	13.46	62.69	6.93	46.37	9.93	21.41	2.07	10.80	1.23	226.33	735.96	574.52	161.44	3.56	12.85	0.90	1.15	0.62	0.79	0.91	0.70	0.85
	kt03-08	80.56	77.30	7.84	33.95	10.40	19.68	13.16	3.49	25.91	5.81	18.07	3.41	22.90	3.08	235.27	325.57	229.73	95.83	2.40	2.52	5.14	0.75	0.65	1.20	1.17	0.88	1.18
	kt03-2-01	104.54	402.08	11.26	69.08	24.38	14.01	35.96	6.48	52.91	11.14	28.38	4.17	21.41	2.38	306.46	788.18	625.34	162.84	3.84	3.50	1.45	2.87	1.09	1.02	1.13	1.06	1.08
	kt03-3-01	131.49	358.85	9.11	53.01	19.67	14.73	30.84	4.13	31.23	7.18	17.14	2.32	10.90	0.94	200.40	691.56	586.87	104.69	5.61	8.65	1.83	2.54	0.94	0.84	1.24	0.89	1.02
	AVERAGE	113.88	485.74	9.01	49.22	17.61	15.61	27.37	4.25	30.99	6.90	17.76	2.47	15.50	1.72	211.38	798.02	691.06	106.95	6.46	5.27	2.17	3.72	1.22	0.92	1.10	1.06	1.01
KT05	kt05-01	18.09	57.30	10.56	54.90	18.74	32.84	26.02	6.91	59.18	14.73	42.76	6.46	38.57	3.95	457.66	391.02	192.44	198.58	0.97	0.34	4.55	1.02	1.08	1.14	1.20	1.11	1.17
	kt05-02	21.09	109.97	11.68	60.82	22.36	25.00	29.63	7.94	67.84	16.01	51.05	7.04	40.91	4.15	498.27	475.48	250.92	224.57	1.12	0.37	2.97	1.72	1.38	1.18	1.15	1.28	1.16
	kt05-03	39.87	91.41	10.49	60.24	21.72	21.07	31.75	8.21	71.67	16.41	50.30	7.04	41.45	4.20	477.19	475.81	244.79	231.02	1.06	0.69	2.45	1.10	0.87	1.18	1.16	1.01	1.17
	kt05-04	25.86	54.05	8.84	53.04	18.71	24.11	29.34	7.25	61.40	13.63	37.77	5.43	34.33	3.68	379.28	377.44	184.61	192.83	0.96	0.54	3.15	0.88	0.81	1.17	1.14	0.98	1.15
	kt05-05	29.12	66.61	7.85	36.08	13.23	22.95	14.60	3.51	32.92	7.21	23.92	4.15	27.89	3.36	281.80	293.40	175.85	117.55	1.50	0.75	5.05	1.08	0.97	1.16	1.18	1.06	1.17
	kt05-06	95.45	299.96	21.31	89.34	31.14	32.52	39.15	10.31	85.20	19.24	54.71	9.31	58.50	6.04	632.75	852.18	569.71	282.47	2.02	1.17	2.85	1.63	1.19	1.20	1.26	1.19	1.23
	kt05-07	53.68	131.03	15.80	91.01	35.38	18.65	55.57	13.52	96.28	22.75	57.96	7.67	37.76	3.83	484.50	640.89	345.56	295.33	1.17	1.02	1.29	1.10	0.90	1.12	1.13	1.00	1.12
	kt05-08	23.71	74.98	9.86	65.71	33.62	15.58	44.97	10.96	93.92	21.28	56.48	7.63	37.18	3.20	473.34	499.08	223.47	275.61	0.81	0.46	1.23	1.20	0.95	1.15	1.23	1.04	1.19
	kt05-09	45.97	148.32	12.38	66.02	22.39	23.91	34.45	7.73	60.78	13.76	39.92	6.10	37.59	3.97	395.71	523.29	318.98	204.31	1.56	0.88	2.63	1.52	1.07	1.10	1.18	1.09	1.14
	AVERAGE	39.20	114.85	12.08	64.13	24.14	24.07	33.94	8.48	69.91	16.11	46.10	6.76	39.35	4.04	453.39	503.18	278.48	224.70	1.24	0.71	2.57	1.29	1.03	1.15	1.18	1.09	1.16
KT06	kt06-01	28.93	51.68	9.99	64.56	31.76	24.54	52.77	13.43	104.88	25.55	65.57	8.95	49.08	4.96	626.81	536.65	211.46	325.19	0.65	0.42	1.83	0.75	0.73	1.13	1.14	0.91	1.14
	kt06-02	50.30	353.28	8.63	58.95	28.78	16.64	50.73	13.06	103.94	25.28	64.15	7.58	35.21	3.11	566.59	819.64	516.59	303.06	1.70	1.02	1.33	4.16	1.40	1.14	1.14	1.26	1.14
	kt06-03	37.90	73.84	10.02	70.04	37.82	17.84	72.18	16.56	130.20	28.95	73.39	8.59	41.81	3.51	615.59	622.62	247.45	375.17	0.66	0.65	1.04	0.93	0.73	1.12	1.16	0.90	1.14
	kt06-04	365.02	118.56	11.98	69.31	27.26	28.55	36.17	9.48	83.14	18.98	52.28	7.76	43.25	4.93	513.21	876.68	620.69	255.99	2.42	6.05	2.78	0.44	0.33	1.19	1.12	0.62	1.15
	kt06-05	41.04	86.70	10.54	64.37	23.45	20.51	38.23	9.91	85.29	18.89	53.25	7.22	41.59	3.75	488.22	504.73	246.60	258.13	0.96	0.71	2.09	1.02	0.81	1.20	1.21	0.99	1.20
	kt06-06	86.18	161.91	5.38	19.55	5.13	18.69	10.46	2.44	18.76	5.31	18.02	3.13	24.65	2.30	231.52	381.91	296.84	85.07	3.49	2.51	7.80	1.84	0.99	1.00	1.35	1.00	1.16
	kt06-07	1026.03	1638.63	6.33	40.23	23.87	20.06	66.38	11.00	96.57	23.37	60.65	7.42	39.70	3.82	532.01	3064.06	2755.14	308.92	8.92	18.54	1.54	4.98	0.69	0.92	1.11	0.80	1.01
	kt06-08	99.90	384.75	22.44	139.67	67.16	30.11	120.96	26.42	190.60	40.30	102.17	12.00	50.91	4.62	833.91	1292.00	744.03	547.98	1.36	1.41	1.02	1.99	1.09	1.12	1.12	1.10	1.12
	kt06-09	105.26	380.89	11.02	67.31	25.23	25.62	40.20	8.11	68.26	16.13	42.71	6.77	41.79	4.03	438.02	843.33	615.32	228.00	2.70	1.81	2.46	2.74	1.06	1.02	1.26	1.04	1.14
	kt06-10	449.30	696.46	18.10	100.68	41.04	27.42	65.88	14.93	116.85	26.95	77.24	9.78	54.77	5.94	724.39	1705.33	1333.00	372.33	3.58	5.88	1.61	1.89	0.73	1.10	1.06	0.89	1.08
	AVERAGE	228.99	394.67	11.44	69.47	31.15	23.00	55.39	12.53	99.85	22.97	60.94	7.92	42.28	4.10	557.03	1064.70	758.71	305.98	2.48	3.89	1.69	1.89	0.74	1.10	1.14	0.90	1.12

https://doi.org/10.3390/min16080782

Table A3. Major and minor elements in scheelite from the Kalasayi tungsten deposit, Western Tianshan, Xinjiang.

(A) Minor elements in scheelite from the Kalasayi tungsten deposit, Western Tianshan, Xinjiang

Project	Sample	Li	Be	B	Sc	V	Cr	Co	Ni	Cu	Zn	Ga	Mo	In	Sn	Cs	Rb	Ba	Th	U	Ta	Nb	Sr	Zr	Hf	Pb
KT01	kt01-01	0.00	0.00	0.30	0.00	4.57	0.00	0.02	0.00	0.00	0.45	2.19	2990.19	0.04	1.80	0.04	0.00	0.23	0.11	0.10	1.14	4.16	101.85	0.02	0.03	6.36
	kt01-02	0.00	0.24	0.00	0.00	0.55	1.22	0.00	0.78	3.90	3.12	0.05	696.37	0.00	0.00	0.00	0.00	0.01	0.11	0.42	1.31	17.06	53.08	0.00	0.00	8.10
	kt01-03	0.00	0.04	1.54	0.00	0.08	1.67	0.00	0.00	0.00	0.33	1.67	7093.76	0.00	0.03	0.00	0.00	0.27	0.18	0.01	1.35	1.39	73.98	0.05	0.04	2.63
	kt01-04	0.00	0.00	0.12	0.00	0.05	0.19	0.00	0.00	0.00	0.19	0.07	6842.06	0.02	0.06	0.00	0.00	0.58	0.08	0.02	1.24	1.42	72.18	0.00	0.00	2.96
	kt01-05	0.00	0.00	0.03	0.00	0.04	1.87	0.00	0.09	0.00	0.08	0.18	7458.57	0.00	0.03	0.00	0.00	0.19	0.07	0.02	1.41	1.51	82.76	0.11	0.00	2.48
	kt01-06	0.00	0.00	0.00	0.00	0.09	0.62	0.00	0.00	0.00	0.00	0.02	1160.54	0.00	0.06	0.00	0.00	0.58	0.09	0.00	1.31	4.81	67.52	0.02	0.08	6.19
	kt01-07	0.00	0.05	0.19	0.00	0.01	0.87	0.00	0.00	0.00	0.38	0.02	930.39	0.00	0.07	0.16	1.51	1.35	0.12	0.01	1.22	5.63	55.28	0.04	0.00	6.96
	kt01-08	0.00	0.00	0.00	0.02	0.16	1.13	0.00	0.06	0.00	0.38	0.06	1687.69	0.00	0.08	0.00	0.00	0.85	0.11	0.03	1.23	3.24	41.01	0.00	0.00	6.58
	KT01-09	0.00	0.00	0.00	0.00	0.08	1.39	0.00	0.00	0.00	0.48	0.11	853.85	0.00	0.05	0.00	0.00	0.31	0.08	0.00	1.24	3.28	60.99	0.00	0.03	4.00
	AVERAGE	0.00	0.04	0.24	0.00	0.62	1.00	0.00	0.10	0.43	0.60	0.49	3301.49	0.01	0.24	0.02	0.17	0.49	0.11	0.07	1.27	4.72	67.63	0.03	0.02	5.14
KT02	kt02-01	0.00	0.02	0.00	0.00	1.21	1.36	0.05	0.84	0.00	2.15	1.31	4699.52	0.00	0.03	0.00	0.00	0.74	0.24	1.87	1.93	101.78	47.83	0.14	0.04	12.32
KT03	kt03-01	0.00	0.33	0.31	0.56	0.08	12.72	0.41	0.00	0.11	2.20	2.56	59.64	0.04	0.29	0.00	0.63	2.76	6.50	3.45	1.57	49.50	280.96	0.25	0.00	14.99
	kt03-02	0.00	0.33	0.34	0.03	0.42	17.24	0.00	0.00	0.00	6.77	2.54	40.78	0.00	0.00	0.00	0.00	3.28	5.06	1.49	1.37	24.94	169.29	0.71	0.13	12.83
	kt03-03	0.58	0.18	2.74	0.33	0.04	18.60	0.01	0.00	0.00	2.16	3.12	37.97	0.00	0.27	0.09	0.00	4.08	6.23	19.57	1.40	13.85	211.51	3.94	0.00	14.76
	kt03-07	0.63	0.80	5.54	1.14	0.26	25.33	0.45	8.76	0.00	5.00	11.59	48.04	0.00	0.29	0.08	0.94	3.96	0.96	2.55	1.21	22.55	142.05	6.19	0.14	9.94
	kt03-08	0.77	0.12	6.56	0.19	0.69	22.78	0.25	0.00	0.00	8.37	27.48	35.59	0.00	0.00	0.03	2.65	9.53	3.56	1.11	1.15	28.42	211.51	11.18	0.26	13.51
	kt03-2-01	1.36	1.77	9.56	0.85	1.77	34.74	0.00	0.87	13.25	10.12	5.22	43.82	0.00	1.04	1.13	3.20	8.14	4.27	3.86	1.59	38.71	311.26	15.94	0.15	41.20
	kt03-3-01	0.24	0.00	6.53	1.00	0.63	21.16	0.00	0.10	0.00	9.15	8.91	40.52	0.20	0.21	0.00	0.41	5.01	3.21	3.50	1.34	76.71	228.88	7.55	0.00	14.41
	AVERAGE	0.51	0.50	4.51	0.59	0.56	21.80	0.16	1.39	1.91	6.25	8.78	43.77	0.04	0.30	0.19	1.12	5.25	4.26	5.08	1.38	36.38	222.21	6.54	0.10	17.38
KT05	kt05-01	0.00	0.00	0.00	0.00	0.13	0.15	0.00	0.12	0.00	2.53	1.33	37.51	0.01	0.08	0.20	0.00	0.44	0.95	0.33	1.74	34.16	181.95	0.31	0.10	15.02
	kt05-02	0.00	1.16	0.38	0.00	0.35	0.18	0.00	0.00	27.70	13.67	1.50	40.48	0.01	0.05	6.38	0.00	0.76	0.82	0.53	1.76	37.38	207.22	1.69	0.07	15.39
	kt05-03	0.00	0.02	0.64	0.22	0.40	1.81	0.00	0.00	3.06	1.80	1.80	34.49	0.00	0.07	0.54	0.00	0.51	1.46	0.79	2.02	49.85	373.73	2.01	0.08	14.16
	kt05-04	0.00	0.00	1.99	0.18	0.19	2.28	0.00	0.00	0.00	0.71	2.00	83.28	0.00	0.08	0.00	0.00	0.98	9.13	6.77	2.21	70.95	325.15	0.47	0.05	13.15
	kt05-05	0.00	0.00	0.83	0.04	0.16	1.78	0.00	0.00	0.00	0.16	1.21	43.62	0.00	0.06	0.00	0.00	1.56	14.17	6.72	1.66	28.90	345.89	0.78	0.16	13.48
	kt05-06	0.00	0.38	1.00	0.00	0.23	1.75	0.00	0.00	0.00	0.20	5.16	46.10	0.03	0.20	0.02	0.00	0.70	8.94	3.18	2.21	55.35	160.03	0.05	0.00	9.18
	kt05-07	0.21	0.28	1.84	0.31	2.32	2.29	0.00	0.17	81.77	6.57	3.78	42.62	0.04	0.20	1.01	0.00	2.07	2.57	0.49	2.06	73.21	192.62	8.09	0.33	15.78
	kt05-08	0.00	0.34	1.78	0.00	0.19	1.38	0.00	0.00	0.00	0.56	1.64	35.88	0.00	0.06	0.00	0.00	0.92	1.42	1.27	1.75	55.68	329.74	0.72	0.00	13.09
	kt05-09	0.00	0.00	1.57	0.06	0.01	0.84	0.04	1.22	0.00	0.01	1.91	41.51	0.00	0.14	0.00	0.00	0.00	6.45	13.27	1.98	36.00	283.67	0.07	0.03	13.18
	AVERAGE	0.02	0.24	1.11	0.09	0.44	1.38	0.01	0.17	12.50	2.91	2.26	45.05	0.01	0.11	0.90	0.00	0.88	5.10	3.71	1.93	49.05	266.67	1.58	0.09	13.60
KT06	kt06-01	0.03	0.00	0.16	0.00	0.29	3.64	0.02	3.09	35.14	1.63	1.61	38.84	0.00	0.03	0.60	0.00	1.48	0.52	0.17	3.63	148.48	297.78	0.49	0.41	15.43
	kt06-02	0.00	0.34	0.62	0.11	0.87	4.80	0.00	0.00	50.24	4.94	3.52	33.02	0.01	0.10	0.73	0.00	1.28	0.29	0.14	3.78	145.19	394.64	1.35	0.33	33.77
	kt06-03	0.00	0.00	0.41	0.00	0.38	3.91	0.00	0.00	0.00	1.29	1.84	42.10	0.00	0.14	0.30	0.00	0.77	0.30	0.24	4.51	189.67	216.57	0.21	0.45	17.97
	kt06-04	0.00	0.00	0.55	0.06	0.20	7.76	0.00	0.68	0.00	1.22	2.62	44.54	0.01	0.70	0.00	0.00	1.31	3.78	4.27	2.40	63.40	196.51	0.02	0.28	16.94
	kt06-05	0.00	0.56	1.44	0.00	1.32	6.96	0.00	0.00	78.19	7.34	2.38	40.45	0.00	0.08	0.85	0.00	1.82	1.04	0.46	1.96	55.05	239.01	1.39	0.10	43.87
	kt06-06	0.00	0.17	0.36	0.06	0.18	6.22	0.00	0.00	0.00	1.19	2.71	44.85	0.00	0.11	0.00	0.00	1.92	0.58	0.21	1.88	17.69	261.44	0.16	0.00	12.73
	kt06-07	0.11	0.13	1.06	0.00	1.14	7.81	0.00	0.00	54.16	5.38	51.50	44.52	0.00	0.05	0.92	0.05	2.28	0.72	0.47	4.23	171.47	400.23	0.73	0.05	22.31
	kt06-08	0.00	0.16	1.07	0.00	0.16	9.93	0.14	0.00	0.00	2.33	8.85	39.50	0.00	0.14	0.00	0.00	4.45	0.52	0.31	3.49	140.51	246.10	0.18	0.43	16.23
	kt06-09	0.00	1.85	4.18	0.38	3.44	5.04	0.57	0.00	234.14	20.71	6.47	42.58	0.04	0.23	3.30	0.00	12.38	3.00	1.54	1.95	41.42	253.18	4.56	0.20	103.84
	kt06-10	0.36	0.70	3.23	0.29	0.59	11.82	0.31	4.60	47.73	5.10	18.46	44.74	0.00	0.46	0.46	0.00	6.19	3.02	1.60	2.30	86.81	184.69	0.65	0.12	19.90
	AVERAGE	0.05	0.39	1.31	0.09	0.86	6.79	0.10	0.84	49.96	5.11	10.00	41.51	0.01	0.21	0.72	0.00	3.39	1.38	0.94	3.01	105.97	269.02	0.97	0.24	30.30

(B) Major elements in scheelite from the Kalasayi tungsten deposit, Western Tianshan, Xinjiang

Project	Sample	Na_2O	MgO	Al_2O_3	SiO_2	P_2O_5	K_2O	CaO	TiO_2	MnO	FeO	WO_3
KT01	kt01-01	0.00	0.03	0.27	0.28	0.00	0.00	24.65	0.00	0.00	0.07	74.22
	kt01-02	0.00	0.00	0.02	0.00	0.00	0.00	24.90	0.00	0.00	0.24	74.70
	kt01-03	0.00	0.00	0.01	0.21	0.00	0.00	26.80	0.00	0.00	0.01	71.87
	kt01-04	0.00	0.00	0.00	0.03	0.00	0.00	25.51	0.00	0.00	0.00	73.41
	kt01-05	0.00	0.01	0.01	0.53	0.01	0.00	26.34	0.00	0.00	0.00	71.97
	kt01-06	0.00	0.00	0.01	0.00	0.00	0.00	25.78	0.00	0.00	0.00	74.02
	kt01-07	0.00	0.00	0.22	0.51	0.00	0.09	25.21	0.00	0.00	0.01	73.81
	kt01-08	0.00	0.00	0.02	0.00	0.00	0.00	24.93	0.00	0.00	0.02	74.76
	KT01-09	0.00	0.00	0.00	0.00	0.00	0.00	24.42	0.00	0.00	0.00	75.44
	AVERAGE	0.00	0.00	0.06	0.17	0.00	0.01	25.39	0.00	0.00	0.04	73.80
KT02	kt02-01	0.00	0.00	0.01	0.00	0.00	0.00	25.58	0.00	0.00	0.00	73.66
KT03	kt03-01	0.12	0.04	0.07	0.69	0.00	0.00	28.28	0.00	0.00	0.01	70.43
	kt03-02	0.71	0.04	0.12	0.65	0.00	0.00	27.77	0.00	0.00	0.01	70.60
	kt03-03	0.57	0.21	0.24	4.48	0.00	0.05	27.53	0.00	0.00	0.03	66.78
	kt03-07	1.35	0.44	0.29	11.44	0.00	0.05	26.19	0.00	0.00	0.04	60.03
	kt03-08	2.53	0.97	0.54	17.20	0.00	0.08	26.09	0.01	0.01	0.05	52.41
	kt03-2-01	2.24	0.58	1.57	14.33	0.02	0.10	31.55	0.00	0.01	0.36	49.02
	kt03-3-01	2.00	0.57	0.34	10.18	0.00	0.08	27.61	0.00	0.00	0.04	59.00
	AVERAGE	1.36	0.41	0.45	8.42	0.01	0.05	27.86	0.00	0.00	0.08	61.18

Table A3. *Cont.*

KT05	kt05-01	0.00	0.00	0.02	0.00	0.00	0.00	24.12	0.00	0.00	0.05	75.66
	kt05-02	0.00	0.01	0.05	0.02	0.01	0.00	23.60	0.00	0.00	0.34	75.81
	kt05-03	0.00	0.01	0.05	0.58	0.01	0.00	23.24	0.00	0.00	0.11	75.82
	kt05-04	0.00	0.00	0.01	0.00	0.00	0.00	23.10	0.00	0.00	0.03	76.70
	kt05-05	0.00	0.00	0.01	0.00	0.00	0.00	25.02	0.00	0.00	0.01	74.83
	kt05-06	0.00	0.00	0.01	0.00	0.00	0.00	24.64	0.00	0.00	0.00	75.12
	kt05-07	0.01	0.02	0.11	0.11	0.03	0.01	24.51	0.00	0.01	0.54	74.45
	kt05-08	0.00	0.00	0.01	0.00	0.00	0.00	24.80	0.00	0.00	0.03	74.98
	kt05-09	0.00	0.00	0.00	0.00	0.00	0.00	23.92	0.00	0.00	0.00	75.91
	AVERAGE	0.00	0.01	0.03	0.08	0.01	0.00	24.11	0.00	0.00	0.12	75.47
KT06	kt06-01	0.00	0.03	0.10	0.03	0.00	0.00	24.76	0.00	0.00	0.03	78.83
	kt06-02	0.00	0.02	0.07	0.08	0.00	0.00	24.94	0.01	0.00	0.41	78.20
	kt06-03	0.00	0.00	0.07	0.00	0.00	0.00	25.42	0.00	0.00	0.06	78.23
	kt06-04	0.00	0.01	0.04	0.00	0.00	0.00	26.29	0.00	0.00	0.04	79.39
	kt06-05	0.00	0.02	0.13	0.02	0.01	0.00	25.68	0.00	0.00	0.48	79.47
	kt06-06	0.00	0.01	0.08	0.01	0.00	0.00	25.62	0.00	0.00	0.00	80.15
	kt06-07	0.00	0.02	0.12	0.05	0.00	0.00	24.97	0.00	0.00	0.16	79.14
	kt06-08	0.00	0.01	0.04	0.00	0.00	0.00	25.00	0.00	0.00	0.01	80.62
	kt06-09	0.01	0.06	0.22	0.55	0.01	0.00	24.29	0.00	0.01	1.46	73.10
	kt06-10	0.02	0.03	0.22	0.11	0.01	0.00	26.42	0.00	0.00	0.10	72.73
	AVERAGE	0.00	0.02	0.11	0.09	0.00	0.00	25.34	0.00	0.00	0.27	77.99

References

1. Şengör, A.M.C.; Natal'in, B.A.; Burtman, V.S. Evolution of the Altaid tectonic collage and Paleozoic crustal growth in Eurasia. *Nature* **1993**, *364*, 299–307. [CrossRef]
2. Xiao, W.; Windley, B.F.; Sun, S.; Li, J.; Huang, B.; Han, C.; Yuan, C.; Chen, H. A tale of two oceans: Accretionary and collisional orogenesis in the Central Asian Orogenic Belt. *Earth-Sci. Rev.* **2015**, *147*, 119–135. [CrossRef]
3. Mao, J.; Li, Y.; Zhang, C.; Pirajno, F. Geology and geodynamics of tungsten deposits in South China. *Ore Geol. Rev.* **2019**, *108*, 345–367. [CrossRef]
4. Zhang, C.; Mao, J.; Yuan, S.; Zhang, H. A-type granites in South China: Implications for tungsten–tin mineralization. *J. Petrol.* **2012**, *53*, 1723–1752. [CrossRef]
5. Chappell, B.W. Aluminium saturation in I- and S-type granites and the characterization of fractionated haplogranites. *Lithos* **1999**, *46*, 535–551. [CrossRef]
6. Yuan, P.; Gu, X.; Zhang, Y. A2-type granite-related deposit: The Kalasayi tungsten deposit, western Tianshan Mountains, Xinjiang, China. *Arab. J. Geosci.* **2022**, *15*, 1002. [CrossRef]
7. Brugger, J.; Lahaye, Y.; Costa, S.; Lambert, D.; Bateman, R. Inhomogeneous distribution of REE in scheelite and dynamics of Archaean hydrothermal systems (Mt. Charlotte and Drysdale gold deposits, Western Australia). *Miner. Depos.* **2000**, *35*, 251–264. [CrossRef]
8. Brugger, J.; Maas, R.; Kamenetsky, V.S. In-situ trace element and Sr–Nd–Pb isotopic characterization of scheelite from the King Island scheelite deposit, Tasmania: Implications for ore-forming processes. *Miner. Depos.* **2000**, *35*, 586–604. [CrossRef]
9. Peng, J.; Hu, R.; Bi, X.; Qin, Y. In-situ LA-ICP-MS trace element analyses of scheelite: Implications for the origin of the quartz-vein type W–Sn deposits in the Nanling Range, South China. *Lithos* **2008**, *105*, 227–240. [CrossRef]
10. Peng, J.; Zhang, D.; Hu, R. Sm–Nd and Sr isotopic geochemistry of scheelite from the Zhazixi W–Sb deposit, western Hunan. *Acta Geol. Sin.* **2008**, *82*, 1512–1520.
11. Wan, Y.; Zhang, H.; Li, G.; Yuan, P.; Liu, G. Geological characteristics and prospecting significance of the Kalasayi tungsten deposit in the West Tianshan Mountains, Xinjiang. *Miner. Explor.* **2016**, *8*, 545–551. [CrossRef]
12. Zhu, D.; Zhao, Z.; Niu, Y.; Hou, Z.; Mo, X. The western Central Asian Orogenic Belt: A window to accretionary orogenesis and continental growth. *J. Asian Earth Sci.* **2014**, *81*, 115–133. [CrossRef]
13. Sun, L.; Ni, S. *Research Report on the Structure of the Zuluhong Tungsten (Copper) Ore Field in the Alatau Mountains*; National 305 Project Office: Urumqi, China, 1988.
14. Wang, K.; Zhou, Y. *Research Report on Material Composition and Geochemistry of the Zuluhong Tungsten (Copper) Deposit in the Alatau Mountains*; National 305 Project Office: Urumqi, China, 1988.
15. Ni, S.; Ma, F.; Chen, J.; Shen, P. Metallization of the Alataw mountains in Xinjiang: Regional setting, source and model. *Chin. J. Geol.* **2009**, *44*, 128–136.
16. Wiedenbeck, M.; Alle, P.; Corfu, F.; Griffin, W.L.; Meier, M.; Oberli, F.; von Quadt, A.; Roddick, J.C.; Spiegel, W. Three natural zircon standards for U-Th-Pb, Lu-Hf, trace element and REE analyses. *Geostand. Geoanal. Res.* **1995**, *19*, 1–23. [CrossRef]
17. Li, Q.L.; Li, X.H.; Liu, Y.; Tang, G.Q.; Yang, J.H.; Zhu, W.G. Precise U–Pb and Pb–Pb dating of Phanerozoic baddeleyite by SIMS with oxygen flooding technique. *J. Anal. At. Spectrom.* **2010**, *25*, 1107–1113. [CrossRef]
18. Morel, M.; Nebel, O.; Nebel-Jacobsen, Y.; Miller, J.; Vroon, P. Hafnium isotope characterization of the GJ–1 zircon reference material by solution and laser-ablation MC–ICP–MS. *Chem. Geol.* **2008**, *255*, 231–235. [CrossRef]
19. Du, A.; Wu, S.; Sun, D.; Wang, S.; Qu, W.; Markey, R.; Stain, H.; Morgan, J.; Malinovskiy, D. Preparation and certification of Re–Os dating reference materials: Molybdenites HLP and JDC. *Geostand. Geoanal. Res.* **2004**, *28*, 41–52. [CrossRef]
20. Smoliar, M.I.; Walker, R.J. Re–Os ages of group IIA, IIIA, IVA, and IVB iron meteorites. *Science* **1996**, *271*, 1099–1102. [CrossRef]
21. Bodnar, R.J. Revised equation and table for determining the freezing point depression of H_2O-NaCl solutions. *Geochim. Cosmochim. Acta* **1993**, *57*, 683–684. [CrossRef]
22. Collins, P.L.F. Gas hydrates in CO_2-bearing fluid inclusions and the use of freezing data for estimation of salinity. *Econ. Geol.* **1979**, *74*, 1435–1444. [CrossRef]
23. Brown, P.E. FLINCOR: A microcomputer program for the reduction and investigation of fluid-inclusion data. *Am. Mineral.* **1989**, *74*, 1390–1393.
24. Gu, X.X.; Peng, Y.W.; Zhang, Y.M.; Xiang, Z.L.; Wang, X.L.; Zhang, Y.S.; Ma, H.D.; Zhu, B.Y.; Dong, S.Y.; Wang, W.; et al. Epithermal Gold Mineralization in the Northern Margin of the West Tianshan, Xinjiang. *Northwest. Geol.* **2026**, *59*, 1–22. [CrossRef]
25. Wen, J.; Hu, A.X.; Peng, J.T. Geochemical Characteristics of Scheelite in the Xi'an Tungsten Deposit, Western Hunan, and Their Implications for Ore Genesis. *Geol. Rev.* **2022**, *68*, 1772–1788. [CrossRef]
26. Whalen, J.B.; Currie, K.L.; Chappell, B.W. A-type granites: Geochemical characteristics, discrimination and petrogenesis. *Contrib. Mineral. Petrol.* **1987**, *95*, 407–419. [CrossRef]
27. Breiter, K.; Ďurišová, J.; Korbelová, Z.; Vašinová Galiová, M.; Hložková, M. Granite Pluton at the Panasqueira Tungsten Deposit, Portugal: Genetic Implications as Revealed from New Geochemical Data. *Minerals* **2023**, *13*, 163. [CrossRef]

28. Fan, K.; Liu, B.; Li, H.; Algeo, T.J.; Vincent, V.I.; Wu, Q. Multistage W-Sn metallogenic processes in the Xitian ore field, South China: Evolution from skarn-type to vein-type mineralization. *Ore Geol. Rev.* **2023**, *158*, 105495. [CrossRef]
29. Han, Y.; Zhao, G. Final Amalgamation of the Tianshan and Junggar Orogenic Collage in the Southwestern Central Asian Orogenic Belt: Constraints on the Closure of the Paleo-Asian Ocean. *Earth-Sci. Rev.* **2018**, *186*, 129–152. [CrossRef]
30. Chen, X.; Shu, L.; Santosh, M. Late Paleozoic post-collisional magmatism in the Eastern Tianshan Belt, Northwest China: New insights from geochemistry, geochronology and petrology of bimodal volcanic rocks. *Lithos* **2011**, *127*, 581–598. [CrossRef]

Disclaimer/Publisher's Note: The statements, opinions and data contained in all publications are solely those of the individual author(s) and contributor(s) and not of MDPI and/or the editor(s). MDPI and/or the editor(s) disclaim responsibility for any injury to people or property resulting from any ideas, methods, instructions or products referred to in the content.